

Contributions to Mineralogy and Petrology

Interpreting titanite U–Pb dates and Zr thermobarometry in high-grade rocks: Empirical constraints on elemental diffusivities of Pb, Al, Fe, Zr, Nb, and Ce --Manuscript Draft--

Manuscript Number:	CTMP-D-18-00270	
Full Title:	Interpreting titanite U–Pb dates and Zr thermobarometry in high-grade rocks: Empirical constraints on elemental diffusivities of Pb, Al, Fe, Zr, Nb, and Ce	
Article Type:	Original Paper	
Keywords:	titanite, U-Pb, geochronology, thermochronology, closure temperature, diffusion	
Corresponding Author:	Robert M Holder Johns Hopkins University Santa Barbara, CA UNITED STATES	
Corresponding Author Secondary Information:		
Corresponding Author's Institution:	Johns Hopkins University	
Corresponding Author's Secondary Institution:		
First Author:	Robert M. Holder	
First Author Secondary Information:		
Order of Authors:	Robert M. Holder	
	Bradley R. Hacker	
	Gareth G.E. Seward	
	Andrew R.C. Kylander-Clark	
Order of Authors Secondary Information:		
Funding Information:	National Science Foundation (EAR-1348003)	Dr Bradley R. Hacker
	National Science Foundation (EAR-1551054)	Dr Bradley R. Hacker
Abstract:	<p>Length scales of compositional heterogeneity in titanite from 800–1000°C metamorphic rocks from southern Madagascar were measured to provide empirical constraints on elemental diffusivities. The calculated Pb diffusivities are comparable to experimental estimates of Sr diffusivity; because of this, U–Pb dates from rocks that reached peak temperatures <850°C should be interpreted as the time of titanite (re)crystallization, not cooling ages. The length scales of Zr diffusion are negligible (<20 μm), even at T >900°C; thus, Zr-in-titanite thermobarometry should not be reset by diffusion in all but the smallest grains in the hottest rocks. Al and Nb diffuse at similar rates to Zr. Ce and Fe diffuse slower than Pb, but faster than Zr. Differences in empirical and experimental estimates of elemental diffusivities might be related to the complexity of most natural titanite solid solutions compared to the near-end-member titanite used in experiments.</p>	

4 1 **Interpreting titanite U–Pb dates and Zr thermobarometry in high-grade rocks: Empirical**
5
6 2 **constraints on elemental diffusivities of Pb, Al, Fe, Zr, Nb, and Ce**

7 3
8
9
10 4 **Contributions to Mineralogy and Petrology**
11 5

12
13 6 Robert M. Holder^{1*}; holder@jhu.edu; ORCID: 0000-0002-1119-6905

14
15 7 Bradley R. Hacker²; hacker@geol.ucsb.edu

16
17 8 Gareth G. E. Seward²; seward@geol.ucsb.edu

18
19 9 Andrew R. C. Kylander-Clark²; kylander@geol.ucsb.edu
20

21 10
22 11 ¹Department of Earth and Planetary Sciences; Johns Hopkins University; Baltimore, MD 21218

23 12 ²Department of Earth Science; University of California; Santa Barbara, CA 93106

24 13 *corresponding author; phone 1-760-920-0406
25 14

26 15 **Abstract**

27 16 Length scales of compositional heterogeneity in titanite from 800–1000°C metamorphic rocks
28 17 from southern Madagascar were measured to provide empirical constraints on elemental
29 18 diffusivities. The calculated Pb diffusivities are comparable to experimental estimates of Sr
30 19 diffusivity; because of this, U–Pb dates from rocks that reached peak temperatures <850°C
31 20 should be interpreted as the time of titanite (re)crystallization, not cooling ages. The length scales
32 21 of Zr diffusion are negligible (<20 μm), even at T >900°C; thus, Zr-in-titanite thermobarometry
33 22 should not be reset by diffusion in all but the smallest grains in the hottest rocks. Al and Nb
34 23 diffuse at similar rates to Zr. Ce and Fe diffuse slower than Pb, but faster than Zr. Differences in
35 24 empirical and experimental estimates of elemental diffusivities might be related to the
36 25 complexity of most natural titanite solid solutions compared to the near-end-member titanite
37 26 used in experiments.
38 27

39
40
41
42
43
44
45 28 **Keywords:** titanite, U–Pb, geochronology, thermochronology, closure temperature, diffusion
46
47
48
49
50
51
52
53
54
55
56
57
58
59
60
61

Introduction

U–Pb titanite ($\text{Ca}[\text{Ti,Al,Fe}^{3+}]\text{SiO}_4[\text{O,OH,F,Cl}]$) dates have been interpreted to record neocrystallization and growth (Corfu, 1996; Kohn and Corrie, 2011; Mottram et al., 2018; Olierook et al., 2018; Scott and St-Onge, 1995; Spencer et al., 2013; Stearns et al., 2016, 2015; Verts et al., 1996), recrystallization during deformation (Bonamici et al., 2015; Spencer et al., 2013), alteration/reaction with a fluid (Corfu, 1996; Garber et al., 2017; Holder and Hacker, 2019; Marsh and Smye, 2017; Olierook et al., 2018), and cooling (Cherniak, 1993; Mattinson, 1978; Mezger et al., 1991; Tucker et al., 1987). The Zr content of titanite has been calibrated as a thermobarometer (Hayden et al., 2008) and titanite commonly contains many other trace elements that can be used to relate dates to physical conditions (pressure, temperature, mineral assemblage) of neocrystallization, growth, dynamic recrystallization, or alteration (Garber et al., 2017). Unlike zircon, titanite reacts with rock-forming minerals, making it useful for conventional thermobarometry (Table 2 of Frost et al., 2001), further allowing U–Pb titanite dates to be tied directly to physical conditions of magmatism and metamorphism (e.g. Scott and St-Onge, 1995). Although titanite is a potentially versatile petrochronometer, interpretations of U–Pb titanite dates are limited by uncertainties in the diffusivities of petrochronologically important elements such as Pb, U, Zr, Al, Fe, Nb, Ta, and REE (see Kohn, 2017, Smye et al., 2018, and Online Resources 1 and 2 for reviews of elemental diffusion in titanite).

Experiments suggest that typical metamorphic titanite grains ($\sim 100\text{-}\mu\text{m}$ diameter cooled at 10 K/Myr) should have a whole-grain closure temperature to Pb diffusion of $\sim 575^\circ\text{C}$ (Cherniak, 1993), to Zr diffusion of $\sim 675^\circ\text{C}$ (Cherniak, 2006), to Nb and Ta diffusion $\sim 725^\circ\text{C}$ (Cherniak, 2015), and to Sr and Nd diffusion of $\sim 800^\circ\text{C}$ (Cherniak, 1995). For Pb, the experimental closure temperature of $\sim 600^\circ\text{C}$ (Cherniak et al., 1993) has been supported by some empirical U–Pb TIMS studies (Mattinson, 1978; Mezger et al., 1993, 1991; Spear and Parrish, 1996; Tucker et al., 2004, 1990, 1987; Verts et al., 1996); however, a growing number of studies by TIMS (Corfu, 1996; Kylander-Clark et al., 2008; Pidgeon et al., 1996; Schärer et al., 1994; Zhang and Schärer, 1996), SIMS (Castelli and Rubatto, 2002; Rubatto and Hermann, 2001), and LA-ICP-MS (Gao et al., 2012; Garber et al., 2017; Kohn and Corrie, 2011; Marsh and Smye, 2017; Mottram et al., 2018; Spencer et al., 2013; Stearns et al., 2016, 2015; Walters and Kohn, 2017) have documented preservation of inherited titanite U–Pb dates and/or heterogeneity in U–Pb dates at the outcrop and grain scales in igneous and granulite-facies-metamorphic rocks that

4 60 require little to no Pb diffusivity in titanite at temperatures as high as 800°C (see Online
5
6 61 Resource 2 for review of empirical studies that have inferred slow Pb diffusion). Although Pb
7
8 62 diffusion has been the focus of most studies, rates of diffusion similar to, or slower than Pb have
9
10 63 also been suggested for other elements, such as Zr (e.g. Stearns et al., 2016; Walters and Kohn,
11
12 64 2017) and the rare-earth elements (REE; e.g. Garber et al., 2017). Two exceptions to the
13
14 65 empirical *in-situ* studies that have hypothesized slow diffusion in titanite are those of Kirkland et
15
16 66 al. (2016) and Bonamici et al. (2015). Kirkland et al. (2016) argued that apparently inherited,
17
18 67 but geologically meaningless U–Pb dates in granulite-facies titanite could result from
19
20 68 preferential U loss relative to radiogenic Pb. Bonamici et al. (2015) interpreted core–rim
21
22 69 covariance in U–Pb dates and $\delta^{18}\text{O}$ in mm-scale granulite-facies titanite grains to record
23
24 70 diffusion during rapid cooling in agreement with the experimental diffusion parameters
25
26 71 (Cherniak, 1993; Zhang et al., 2006).

26 72 Whereas many studies have suggested limited elemental diffusivity in titanite, the diffusivity
27
28 73 estimates of these studies are semi-quantitative, based on the preservation of compositional and
29
30 74 isotopic heterogeneity (or lack thereof) within and among titanite grains, rather than the
31
32 75 quantification of diffusion profiles. Furthermore, the available empirical constraints on elemental
33
34 76 diffusivity in titanite are all from rocks of similar temperature: 700–800°C. In this study, both of
35
36 77 these limitations are addressed through the calculation of elemental diffusivities of Zr, Nb, Ce,
37
38 78 Al, Fe, and Pb in titanite as a function of the length scales of preserved compositional gradients
39
40 79 in titanite—interpreted to be arrested diffusion profiles—from 800–1000°C calc-silicate gneisses
41
42 80 from southern Madagascar.

42 81

44 82 **Studied samples**

46 83 Two titanite-bearing samples were chosen from the gneisses of southern Madagascar that were
47
48 84 metamorphosed during the Ediacaran–Cambrian continental collision between East and West
49
50 85 Gondwana (Fig. 1: Collins et al., 2012; Tucker et al., 2014; Boger et al., 2015; Fitzsimons,
51
52 86 2016). Titanite 12D is from a calc-silicate gneiss exposed in a road cut ~12 km west of
53
54 87 Ankaramena in the Ikalamavony Domain (location: 46.5498, -21.9645). The gneiss consists of
55
56 88 clinopyroxene, plagioclase, scapolite, quartz, Ca-amphibole, titanite, calcite, epidote, minor
57
58 89 garnet, minor magnetite, minor apatite, and trace zircon. Grains are typically equant and
59
60 90 xenoblastic, except that amphibole and titanite are (hyp)idioblastic. Foliation is defined by

4 91 alternating layers of pyroxene–amphibole rich and poor layers. Finer-grained Ca-amphibole,
5
6 92 epidote, chlorite, calcite, and white mica occur interstitially, along grain boundaries, and as
7
8 93 coronae and pseudomorphs after other phases (mainly clinopyroxene); these features are
9
10 94 interpreted to be retrograde. The studied titanite is a 0.5 cm euhedral grain separated from a
11
12 95 coarser clinopyroxene–amphibole-poor layer. Peak metamorphic temperature is inferred to have
13
14 96 been 750–800°C, based on Zr-in-titanite thermometry and the inferred peak-*T* assemblage
15 97 clinopyroxene–Ca-amphibole–calcite (Holder and Hacker, 2019). For additional information on
16
17 98 the thermal history of this region, see Grégoire et al. (2009) and Ganne et al. (2014). A different
18
19 99 cm-sized titanite grain from this outcrop was studied by Holder and Hacker (2019) to determine
20
21 100 the efficiency of fluid–titanite interaction in resetting U–Pb titanite dates.

22 101 Titanite 21B is from a calc-silicate gneiss collected across the river from the Gendarmerie in
23
24 102 Tranomaro in the Anosyen Domain (location: 46.4757, -24.5989). The sample contains two
25
26 103 spatially distinct mineral assemblages: (1) clinopyroxene, scapolite, titanite, quartz, plagioclase,
27
28 104 wollastonite, minor apatite, and trace zircon and (2) clinopyroxene, scapolite, titanite, quartz,
29
30 105 plagioclase, alkali-feldspar, epidote, minor apatite, and trace zircon. Scapolite–quartz
31
32 106 symplectites along the contact between the two mineral assemblages suggest they are not in
33
34 107 equilibrium. In mineral assemblage 1, calcite and quartz occur around and along fractures
35 108 through wollastonite and are interpreted to be the result of retrogression. The presence of epidote
36
37 109 in mineral assemblage 2, along with the symplectite along the boundary of the two mineral
38
39 110 assemblages suggests that it crystallized at a lower temperature, probably associated with post-
40
41 111 peak-temperature “stage 2” metasomatism (Rakotondrazafy et al., 1996). Titanite
42
43 112 petrochronology from mineral assemblage 2 was studied by Holder and Hacker (2019) to
44
45 113 determine the efficiency of fluid-titanite interaction for resetting U–Pb titanite dates during
46
47 114 retrogression. This study examines a single large titanite grain from mineral assemblage 1, which
48
49 115 is interpreted to have equilibrated at or near the peak metamorphic temperature, based on the
50 116 assemblage wollastonite–quartz. The peak metamorphic temperature is estimated to have been
51
52 117 900–1000°C based on pseudosections (Boger et al., 2012; Holder et al., 2018a), feldspar-solvus
53
54 118 thermometry (Holder et al., 2018a), Al in orthopyroxene (Jöns and Schenk, 2011), Zr in rutile
55
56 119 and Ti in quartz (Horton et al., 2016), Zr in titanite (Holder and Hacker, 2019), oxygen-isotope
57 120 thermometry (Holder et al., 2018b), and the widespread stability of (ultra)high-temperature
58
59 121 mineral assemblages (sapphirine–quartz, orthopyroxene–sillimanite–quartz: Jöns and Schenk,
60
61

2011; osumilite, Al-spinel–quartz: Holder et al., 2018a; Jöns and Schenk, 2011). For additional information on the thermal history of this region, see Holder et al. (2018a).

Methods

Laser-ablation split-stream inductively coupled plasma mass spectrometry (LASS)

One thousand twenty-six LASS spot analyses were conducted on a single titanite grain in a thin section from sample 21B to assess grain-scale heterogeneity in U–Pb dates. Dates and trace-element compositions were measured using the split-stream procedure described by Kylander-Clark et al. (2013) and Kylander-Clark (2017) at the University of California, Santa Barbara.

Four LASS depth profiles were measured perpendicular to a titanite crystal face in sample 12D to evaluate possible Pb diffusion out of titanite. The titanite was then cut perpendicular to the measured crystal face after laser ablation to measure the pit depths (19 μm) and to map near-rim Zr, Nb, Ce, Al, and Fe concentrations in two dimensions by EPMA (see *Quantified EPMA trace-element maps*) as a complement to the one-dimensional LASS data. The methods used to acquire and process the depth profile data, along with an assessment of data precision and accuracy, are given in Online Resource 3. The precision of each datum in each depth profile is: 5.1% for $^{207}\text{Pb}/^{235}\text{U}$, 4.3% for $^{206}\text{Pb}/^{238}\text{U}$, 2.0% for $^{207}\text{Pb}/^{206}\text{Pb}$, and 7.5% for $^{208}\text{Pb}/^{232}\text{Th}$ (95% confidence interval). All four depth profiles yielded consistent results; the 2-standard-error of the weighted mean of the four depth profiles is: 2.6% for $^{207}\text{Pb}/^{235}\text{U}$, 2.2% for $^{206}\text{Pb}/^{238}\text{U}$, 1.0% for $^{207}\text{Pb}/^{206}\text{Pb}$, and 3.8% for $^{208}\text{Pb}/^{232}\text{Th}$. Secondary-reference-material reproducibility for the depth profiles was $\leq 1.5\%$, suggesting that the accuracy of the depth profiles is comparable to the accuracy of traditional LASS spot analyses: 1–2% (Košler et al., 2013; Spencer et al., 2013).

Quantified EPMA trace-element maps

The elemental concentrations of Al, Fe, Zr, Nb, and Ce were mapped parallel to the LASS depth profiles in titanite 12D (after cutting the grain perpendicular to the profiled crystal face; Fig. 2) and in a single large titanite grain in thin section (titanite 21B) using a Cameca SX100 EPMA at the University of California, Santa Barbara. The beam current was 200 nA. The accelerating voltage was 15 kV. The counting time per pixel was 1 s. The activation volume (the region from which 95% of X-rays were generated) under these beam conditions was estimated to have been 1.5 μm in diameter using the program CASINO. The maps of titanite 21B were collected using a

4 153 10 μm pixel spacing, and those collected parallel to the depth profiles in titanite 12D using a 1
5
6 154 μm pixel spacing (slightly smaller than the 1.5 μm activation volume). LPET crystals were used
7
8 155 to measure Zr and Nb L_{α} X-rays, LLIF crystals for Fe K_{α} and Ce L_{α} , and a TAP crystal for Al K_{α} .
9
10 156 The maps were processed using Calc Image of the Probe for EPMA software. The weight
11
12 157 percent of each element was calculated from the counts-per-second per nA of each pixel in the
13
14 158 maps using a mean-atomic-number background calibration (Donovan et al., 2016) and ZAF
15
16 159 correction assuming that the matrix composition was CaTiSiO_5 . Because this approach to
17
18 160 quantifying EPMA maps is not yet widely used, the accuracy of the method is demonstrated, as a
19
20 161 proof-of-concept, by direct comparison of quantified map pixels with spot analyses from the
21
22 162 same location (Fig. 3). The spot-analysis beam current was 40 nA, the accelerating voltage was
23
24 163 15kV, and the beam diameter was 10 μm . The elements F, Na, Al, Si, Cl, Ca, Mn, Fe, Zr, Nb, Ce
25
26 164 were measured; Cl and Na were below detection limit in all analyses. Additional details of the
27
28 165 data collection are given in Online Resource 4. Representative EPMA spot analyses are shown in
29
30 166 Table 1. All spot analyses are presented in Online Resource 5 and the corresponding map pixel
31
32 167 values are presented in Online Resource 6.

33 168 34 169 **Results**

35 170 Due to the large amount of data used in this study, only representative EPMA spot analyses are
36
37 171 presented in the main text of this paper (Table 1). The rest of the data are available in .xlsx
38
39 172 format in Online Resources 5–11.

40 173 41 42 174 **800°C titanite 12D**

43
44 175 Four U/Th–Pb+Zr LASS depth profiles were measured by ablating into the crystal face of titanite
45
46 176 12D (Figs. 3–5; Online Resource 7); afterward, the titanite was cut perpendicular to that crystal
47
48 177 face, polished until two of the LASS pits were partially exposed, and mapped by EPMA for Al,
49
50 178 Fe, Zr, Nb, and Ce (Fig. 6). Compositional gradients were extracted as swath profiles (averages
51
52 179 of parallel line profiles) from the area between the two exposed laser pits in the EPMA maps
53
54 180 (Online Resource 8).

55 181 LASS depth profiles (Figs. 4, 5) of titanite 12D show downhole increases *and* decreases in U,
56
57 182 Th, and individual Pb isotopes within the same pit. The ^{206}Pb and ^{207}Pb profiles mimic the shape
58
59 183 of the U profile and the ^{208}Pb profile mimics the shape of the Th profile, as expected for a system

4 184 that has remained largely closed since 500 Ma. However, the $^{206}\text{Pb}/^{238}\text{U}$, $^{207}\text{Pb}/^{235}\text{U}$, $^{208}\text{Pb}/^{232}\text{Th}$,
5
6 185 and ^{207}Pb -corrected $^{206}\text{Pb}/^{238}\text{U}$ date (corrected using the $^{207}\text{Pb}/^{206}\text{Pb}$ composition of
7
8 186 clinopyroxene from the same rock; Online Resource 9) profiles decrease toward the grain rim,
9
10 187 corresponding to younger dates. The dates decrease gradually from 550 ± 12 to 535 ± 12 Ma (2se
11
12 188 of the weighted mean of the four adjacent depth profiles) between the bottom of the pit and $5 \mu\text{m}$
13
14 189 depth, then decrease more rapidly to 495 ± 11 Ma at the crystal face.

15 190 The EPMA maps and extracted swath profiles of Al, Fe, Zr, Nb, and Ce are shown in Fig. 6.
16
17 191 Zr, Al, and Fe all decrease monotonically toward the crystal face of titanite 12D; no clear
18
19 192 diffusion profiles are present. The Nb and Ce concentrations increase toward the crystal face
20
21 193 within the outermost 6 and $20 \mu\text{m}$ of the profile, respectively, possibly the result of diffusive
22
23 194 influx or growth zoning.

24 195 25 26 196 **900–1000°C titanite 21B**

27
28 197 EPMA maps of Al, Fe, Zr, Nb, and Ce and a LASS map of U–Pb dates in titanite 21B are shown
29
30 198 in Fig. 7. A larger version of the U–Pb map, with surrounding phases annotated, is shown in Fig.
31
32 199 8. The LASS spot analyses that define the U–Pb map are presented in Online Resource 10.

33 200 Elemental zoning, best seen in Zr, is characterized by: 1) gradual changes in composition at
34
35 201 the mm scale, and 2) sharp ($10\text{--}100 \mu\text{m}$ scale) compositional steps. The sharp compositional
36
37 202 gradients are similar to those documented by Holder and Hacker (2019) for titanite throughout
38
39 203 the Anosyen domain; they were interpreted to have formed by interface-coupled dissolution–
40
41 204 precipitation (replacement of precursor titanite by titanite of different composition).
42
43 205 Compositional gradients in Al, Fe, Zr, Nb, and Ce were extracted from three of these sharp
44
45 206 compositional steps as swath profiles (averages of parallel line profiles). The swath profiles are
46
47 207 shown in Fig. 9; data for the profiles is presented in Online Resource 11. The length scales of the
48
49 208 compositional gradients in Zr, Al, and Nb across these profiles are $\sim 40 \mu\text{m}$. The length scales of
50
51 209 the compositional gradients in Ce range from $40\text{--}120 \mu\text{m}$. The length scales of compositional
52
53 210 gradients in Fe are $50\text{--}150 \mu\text{m}$. These relatively sharp compositional steps are all associated with
54
55 211 the regions of highest Zr concentrations.

56 212 The LASS map of titanite 21B1 (Fig. 8) shows U–Pb dates from 545 ± 11 Ma to 490 ± 10
57
58 213 Ma (spot analyses corrected for common Pb using the $^{207}\text{Pb}/^{206}\text{Pb}$ composition of clinopyroxene;
59
60 214 Online Resource 9). Three domains of distinctly older U–Pb dates were observed, each $\sim 200\text{--}$
61

300 μm in radius/half-width. Whereas the majority of U–Pb titanite dates in the Anosyen domain are <530 Ma and interpreted to record low-temperature retrogression (Holder and Hacker, 2019), the oldest dates from titanite 21B1 agree with the age of peak metamorphism (550 ± 11 Ma; Holder et al., 2018a). The spread of dates from 545 to 490 Ma coincides with abundant monazite and zircon dates from pelitic and felsic gneisses (Holder et al., 2018a; Horton et al., 2016; Jöns and Schenk, 2011) and widespread partial melt crystallization (Collins et al., 2012; Jöns and Schenk, 2011; Paquette et al., 1994; Tucker et al., 2011) interpreted to reflect cooling of the terrane (Holder et al., 2018a) and local hydrothermal fluid circulation (Holder and Hacker, 2019).

Discussion

Estimate of Pb diffusivity in titanite 12D

The U–Pb date decreases by 30–40 Myr within the outermost 5 μm of the depth profile. This could reflect (1) loss of Pb by volume diffusion or (2) protracted growth, as suggested by Stearns et al. (2016) for near-rim zoning in titanite from gneiss domes in the Pamir Mountains. If the profile reflects volume diffusion, assuming a conservative range of 1–40 Myr for the duration of near-peak-temperature metamorphism (750–800°C; Holder and Hacker, 2019), the Pb diffusivity is calculated to be $10^{-24.7}$ – $10^{-26.2}$ m^2/s (Table 2; Fig. 10) using the equation for the characteristic length-scale of diffusion: $u = 2\mathcal{N}(Dt)$ (u the diffusion length scale, D diffusivity, and t time at peak temperature). This simple equation was used because the complex zoning of U observed in the depth profile does not permit an error-function fit, although the approximate length-scale of the near-rim zoning from diffusion should still be similar (see Smye et al., 2018). This estimate for Pb diffusivity agrees with extrapolated values of experimental Sr diffusivity (hypothesized to be a reasonable approximation of Pb diffusivity in natural titanite; Kohn, 2017), but is significantly slower than experimental Pb diffusivity (Cherniak, 1993). If some of the U–Pb zoning reflects protracted growth, this estimate of Pb diffusivity is a maximum.

Estimates of Al, Fe, Zr, Nb, and Ce diffusivities in titanite 12D

Zr, Al, and Fe all decrease monotonically toward the crystal face of titanite 12D; no clear diffusion profiles are present, suggesting that the length scale of diffusion was shorter than the analytical resolution of the maps (1.5 μm). Based on a conservative range of durations of near-

4 246 peak-temperature metamorphism (1–40 Myr; the same as that used for the Pb diffusion
5
6 247 estimates) the diffusivities for these elements at ~800°C must be less than $10^{-25.8}$ – $10^{-27.4}$ m²/s (u
7
8 248 = $2\sqrt{Dt}$); Table 2; Fig. 10). The Nb concentrations increase toward the crystal face within the
9
10 249 outermost 6 μm of the profile. If this is the result of diffusive influx, rather than growth, this
11
12 250 corresponds to a diffusivity of $10^{-24.5}$ – $10^{-26.2}$ m²/s (Table 2; Fig. 10). Ce increases gradually
13
14 251 toward the crystal face within the outermost 20 μm of the profile. If this is the result of diffusive
15
16 252 influx, rather than growth, this corresponds to a diffusivity of $10^{-23.5}$ – $10^{-25.1}$ m²/s (Table 2; Fig.
17
18 253 10). However, the absence of Zr, Al, or Fe diffusion profiles suggests that the Ce and Nb profiles
19
20 254 might simply reflect growth zoning (similar to the interpretation of near-rim zoning in the depth
21
22 255 profiles of Stearns et al., 2016), in which case the estimated diffusivities of Nb and Ce are
23
24 256 maxima.

257 26 258 **Estimate of Pb diffusivity in titanite 21B**

27
28 259 The LASS map of titanite 12B1 (Fig. 8) shows U–Pb dates from 545 ± 12 Ma to 490 ± 11 Ma
29
30 260 (spot analyses corrected for common Pb using the $^{207}\text{Pb}/^{206}\text{Pb}$ composition of clinopyroxene).
31
32 261 The oldest dates agree with the age of peak metamorphism in the Anosyen Domain (550 ± 11
33
34 262 Ma; Holder et al., 2018a); the youngest dates correspond to cooling, retrogression, and
35
36 263 widespread hydrothermal circulation during retrogression (Holder and Hacker, 2019). The
37
38 264 isotopically older domains within the titanite have radii/half-widths of 200–300 μm. For a length
39
40 265 scale of 200–300 μm, a peak temperature of 900–1000 °C (Jöns and Schenk, 2011; Boger et al.,
41
42 266 2012; Horton et al., 2016; Holder et al., 2018a,b; Zr-in-titanite T , this study), and a timespan of
43
44 267 1–20 Myr for peak metamorphism (Holder et al., 2018a), the calculated Pb diffusivity is $10^{-20.5}$ –
45
46 268 $10^{-21.9}$ m²/s (Table 2; Fig. 10). This value is equivalent to estimates of Sr diffusivity from the
47
48 269 experiments of Cherniak (1995), and consistent with the hypothesis of Kohn (2017) that
49
50 270 experiments for Sr diffusivity provide reasonable estimates of Pb diffusivity.

51
52 271 Although the length scale of Pb diffusion *within* Madagascar titanite is consistent with
53
54 272 experimental estimates for Sr diffusivity, the distribution of U–Pb dates within the grain suggest
55
56 273 that diffusion of Pb out of titanite might not have occurred at the same rate everywhere. The
57
58 274 titanite dates do not simply decrease from core to rim (Fig. 8), but rather, three regions of older
59
60 275 dates are preserved. Some of the oldest dates (c. 545 Ma) are within 200 μm of the grain rim.
61
62 276 (All of these data have been screened using trace-element concentrations to remove the effects of

4 277 small impurities such as zircon or monazite.) Holder and Hacker (2019) discussed the
5
6 278 importance of interface-coupled dissolution–precipitation reactions (ICDR), rather than volume
7
8 279 diffusion, for resetting other titanite grains in Madagascar during retrogression; however, the
9
10 280 lack of correlation between U–Pb dates and elemental zoning suggests that ICDR cannot be the
11
12 281 sole explanation for the irregular distribution of U–Pb dates in this titanite. Alternatively, the
13
14 282 irregular distribution of U–Pb dates might indicate that: 1) diffusion of Pb out of titanite
15
16 283 depended on grain-boundary conditions, such as the availability of a fluid phase or the phase
17
18 284 adjacent to titanite (see Kohn et al., 2016, and Smye et al., 2018, for discussions of possibly
19
20 285 grain boundary effects on the preservation of U–Pb dates), 2) that Pb diffusion rates in titanite
21
22 286 were not the same everywhere due to fast-diffusion pathways, such as those documented for
23
24 287 oxygen diffusion in experiments (Zhang et al., 2006), or those discussed for cation diffusion by
25
26 288 Marsh and Smye (2017) and Smye et al. (2018), and/or 3) the titanite grain might have grown
27
28 289 and/or been resorbed during cooling—as suggested by its xenoblastic habit—resulting in a
29
30 290 moving grain boundary during or after Pb diffusion. Differentiating among these hypotheses is
31
32 291 beyond the scope of this study, but they are pointed out to highlight the complexities of
33
34 292 interpreting elemental and isotopic zoning titanite.

35 294 **Estimates of Al, Fe, Zr, Nb, and Ce diffusivities in titanite 21B**

37 295 In titanite 21B, three steep compositional gradients were chosen to calculate elemental
38
39 296 diffusivities (locations marked with stars in Fig. 7; swath profiles shown in Fig. 9). Due to the
40
41 297 possible complications of grain-boundary effects mentioned in the previous paragraph, profiles
42
43 298 internal to the titanite, rather than grain-boundary profiles, were chosen. The steep (10–100- μm
44
45 299 scale) compositional gradients were chosen over the more-gradual (mm-scale) compositional
46
47 300 gradients, because the shortest length scales of compositional heterogeneity provide the strongest
48
49 301 constraints on diffusivity (e.g. 10–100 μm compositional gradients cannot be preserved if the
50
51 302 length-scale of diffusion is 1 mm). Assuming that these steep compositional gradients began as
52
53 303 step functions and that the rock cooled linearly from the time that each of the step functions
54
55 304 formed, diffusion parameters for Al, Fe, Zr, Nb, and Ce were calculated using the following
56
57 305 equation from Watson and Cherniak (2015):

$$38 \log_{10} S_0 = 2.504 - \frac{1}{2} \log_{10} D_0 - \log_{10} T_i + \frac{1}{2} \log_{10} E_a - \frac{1}{2} \log_{10} \dot{T} + \left(26.11 \frac{E_a}{\dot{T}} \right)$$

4 307 where S_0 is the slope at the center of the best-fit (least-squares) error function (normalized such
5
6 308 that the maximum value of the error function is 100 and the minimum value is 0); T_i the
7
8 309 temperature (K) at which the compositional step formed and cooling began; \dot{T} the cooling rate
9
10 310 (K/s); and D_0 (m²/s) and E_a (kJ/mol) the elemental diffusivity at infinite temperature and the
11
12 311 activation energy of diffusion, respectively. D_0 and E_a describe the temperature dependence of
13
14 312 elemental diffusivity D by the Arrhenius relationship, $D = D_0 e^{-E_a/RT}$ (R , the gas constant). The
15
16 313 cooling rate used for the calculations was 17 ± 7 K/Myr, constrained by monazite petrochronology
17
18 314 (Holder et al., 2018a) and U/Th–He monazite dates (Montel et al., 2018); for discussion of the
19
20 315 thermal history of the Anosyen Domain, see Holder et al. (2018a). The T_i used for the
21
22 316 calculations are described below.

23 317 Because there are two unknown diffusion parameters, D_0 and E_a , the calculated value of each
24
25 318 can only be described as a function of the other. It was found that permissible values of D_0 and
26
27 319 E_a are related by $\log_{10} D_0 = m \times E_a + b$. Uncertainties in S_0 (as a function of analytical
28
29 320 uncertainties in the swath profiles), T_i (next paragraph), and \dot{T} (17 ± 7 K/Myr; Holder et al.,
30
31 321 2018a) were propagated into uncertainties in m and b by Monte Carlo analysis. All uncertainties
32
33 322 presented are 95% confidence intervals. Implicit in these calculations is that the chemical
34
35 323 potential of each element is proportional to its concentration; this is a reasonable assumption
36
37 324 based on the low concentrations of each element (~ 2.0 wt.% Al; ~ 1.4 wt.% Fe; < 1 wt.% each of
38
39 325 Ce, Nb, and Zr) and their limited compositional ranges (± 1000 ppm Al and Fe, ± 500 ppm Ce,
40
41 326 ± 200 – 400 ppm Nb, ± 3000 – 5000 ppm Zr).

42 327 For each element in each profile, two calculations were made starting with the Zr-in-titanite
43
44 328 temperatures from either side of the compositional steps as T_i . Uncertainties used for T_i are the
45
46 329 propagated uncertainties of the coefficients of the experimental calibration of the Zr-in-titanite
47
48 330 thermobarometer (Hayden et al., 2008), uncertainty in the pressure of metamorphism (0.6 ± 0.2
49
50 331 GPa; Holder et al., 2018a), and a conservatively large uncertainty in a_{TiO_2} (0.75 ± 0.25) reflecting
51
52 332 the absence of rutile in the samples, but recognizing that a_{TiO_2} is likely greater than 0.5 in titanite-
53
54 333 bearing rocks (Chambers and Kohn, 2012; Ghent and Stout, 1984). The highest T_i was
55
56 334 $956 \pm 64^\circ\text{C}$, the lowest $873 \pm 57^\circ\text{C}$ (Table 2). As stated in the previous paragraph, the uncertainties
57
58 335 in these T_i values were propagated through the calculations by Monte-Carlo analysis, along with
59
60 336 uncertainties in the cooling rates, and in the elemental concentrations extracted from the
61
62 337 quantified maps. The large uncertainties in T_i contribute to order-of-magnitude uncertainties in

4 338 calculated elemental diffusivities, but ensure that the results are not strongly biased toward a
5
6 339 single interpretation of the thermal history. For example, the highest T_i is consistent with the
7
8 340 inferred peak metamorphic temperature of Holder et al. (~950°C; 2018a,b), Horton et al. (2016),
9
10 341 and Jöns and Schenk (2011), whereas the lowest T_i is consistent with the inferred peak
11
12 342 temperature of Rakotondrazafy et al. ($\geq 850^\circ\text{C}$; 1996), and both are consistent with the peak
13
14 343 metamorphic temperature of Boger et al. (880–920°C; 2012).

15 344 The calculations presented in this section assume that the steep compositional gradients
16
17 345 formed at or near the peak metamorphic temperature. This assumption is based on the
18
19 346 preservation of both Zr temperatures and U–Pb dates that are consistent with independent
20
21 347 estimates of the temperature and timing of peak metamorphism (previous paragraph; Holder et
22
23 348 al., 2018a, and references therein). It is noted, however, that the sharp profiles used for diffusion
24
25 349 modeling occur at the edge of irregularly shaped, lobate compositional domains. The lobate
26
27 350 shapes of the domains and their relatively sharp compositional boundaries are consistent with
28
29 351 formation by ICDR (Putnis, 2009) in which precursor titanite was replaced by titanite of
30
31 352 different composition. If the zoning formed by such reactions, and if titanite–zircon equilibrium
32
33 353 was not achieved during formation of the new domains (as suggested for some titanite by Holder
34
35 354 and Hacker, 2019), the profiles might have formed at lower temperature than indicated by Zr
36
37 355 thermobarometry and the calculated diffusivities would not be accurate. However, as discussed
38
39 356 below, the calculations for Zr diffusivity in titanite 21B (the most studied of the elements Al, Fe,
40
41 357 Zr, Nb, and Ce) are consistent with the maximum diffusivities estimated by other empirical
42
43 358 studies (Kohn, 2017; Stearns et al., 2016; Walters and Kohn, 2017). Furthermore, the diffusivity
44
45 359 estimates for all elements in titanite 21B agree, within uncertainties, with those in titanite 12D
46
47 360 (Fig. 10). While there will always be geological uncertainty in the calculation of empirical
48
49 361 physical properties (like diffusivities or partitioning coefficients) the consistency of empirical
50
51 362 diffusivities calculated from different samples and in different studies suggests that the assumed
52
53 363 thermal history used in these calculations is appropriate.

54 364 Best-fit error functions are shown in Fig. 9. Calculated diffusion parameters are shown in
55
56 365 Fig. 10 and Table 2. The estimates of elemental diffusivity extracted from these profiles are
57
58 366 maxima, because the modeled compositional boundaries are likely not perpendicular to the thin
59
60 367 section, resulting in apparent length scales of diffusion greater than the true length scales.

4 368 The estimates for maximum Zr diffusivity are $\sim 4 \pm 1$ orders of magnitude slower than the
5
6 369 experimental results of Cherniak (2006). This is consistent with the common preservation of
7
8 370 granulite- or high-temperature eclogite-facies Zr-in-titanite temperatures in many terranes (Gao
9
10 371 et al., 2012; Garber et al., 2017; Kirkland et al., 2016; Kohn and Corrie, 2011; Mottram et al.,
11
12 372 2018; Olierook et al., 2018; Spencer et al., 2013). It is also consistent with the preservation of
13
14 373 sector zoning (μm -scale) in $\sim 800^\circ\text{C}$ titanite in the Greater Himalayan Sequence (Walters and
15
16 374 Kohn, 2017), and the absence of inferred diffusion at the sub- μm scale in depth profiles of 750–
17
18 375 800°C titanite from gneiss domes in the Pamir Mountains (Stearns et al., 2016).

19 376 The estimates for maximum Nb diffusivity are $\sim 3 \pm 2$ orders of magnitude slower than
20
21 377 experiments (Cherniak, 2015). The individual estimates for maximum Al diffusivity range from
22
23 378 the same as experimental Nd diffusivity within uncertainty (at FMQ: Cherniak, 1995) to 2 ± 1
24
25 379 orders of magnitude slower than experimental Nd diffusivity and $3\text{--}4 \pm 1$ orders of magnitude
26
27 380 slower than experimental Nb–Ta diffusivity (Cherniak, 2015). In the Nd and Nb diffusion
28
29 381 experiments, each was diffusively coupled to Al. Surprisingly, the calculated diffusivities of Nb
30
31 382 and Al—which rely on coupled substitutions—are the same as those of Zr, within uncertainty,
32
33 383 which is thought to enter titanite by the simple substitution mechanism $\text{Zr}^{4+} = \text{Ti}^{4+}$ (Hayden et
34
35 384 al., 2008).

36 385 The estimates for maximum Ce diffusivity are the same as, or within one order of magnitude
37
38 386 of, the experimental Nd diffusivity measured at the FMQ buffer (Cherniak, 1995). This
39
40 387 agreement is consistent with the predicted similarities in geochemical behavior of the REE, but
41
42 388 significant in that Ce has two common valence states (Ce^{4+} and Ce^{3+}) that likely diffuse by
43
44 389 different mechanisms and at different rates. Due to differences in Ce valence, Ce diffusivity is
45
46 390 likely to be influenced by $f\text{O}_2$.

47 391 Fe exhibits the largest and most variable length scales of compositional variation. Fe is
48
49 392 commonly assumed to substitute into titanite by the same mechanism as Al— $(\text{Al}, \text{Fe}^{3+}) + (\text{F}^-$
50
51 393 $, \text{OH}^-) = \text{Ti}^{4+} + \text{O}^{2-}$ —and therefore might be expected to have an elemental diffusivity similar to
52
53 394 Al. However, Fe gradients are $>3\text{x}$ longer than the Al gradients, corresponding to a weighted
54
55 395 average difference between calculated D_{Fe} and D_{Al} of 1.4 ± 0.6 orders of magnitude (2se). This
56
57 396 may be explained, in part, by the presence of some Fe^{2+} in titanite, rather than pure Fe^{3+} as
58
59 397 commonly assumed (e.g. Franz and Spear, 1985): Fe^{2+} would likely diffuse faster than Fe^{3+} due
60
61

4 398 to its lower charge. If titanite accommodates Fe²⁺ and Fe³⁺, the diffusivity of Fe is likely to be
5
6 399 influenced by fO_2 .

7
8 400
9
10 401 **Differences among empirical and experimental diffusivity estimates in titanite: the possible**
11 402 **role of coupled substitutions and differences in titanite compositions**

12
13 403 The purpose of this study is to provide empirical constraints on elemental diffusion in titanite. As
14
15 404 with previous empirical studies, the elemental diffusion rates of Pb and Zr were found to be
16
17 405 slower than in experiments. Nb diffusion was also found to be slower than experiments. This
18
19 406 section discusses chemical and physical differences between the titanite used in experiments and
20
21 407 most natural titanite that might explain the reported differences in elemental diffusivities.

22 408 A notable difference between the empirical and experimental studies of elemental diffusion
23
24 409 in titanite is that the experimental studies have used near-end-member CaTiSiO₅—as evident
25
26 410 from its pale green color, minimal Al–Fe content, and near 100 wt.% totals for EPMA
27
28 411 measurements of major elements (Online Resource 1)—whereas most titanite used for
29
30 412 geochronology is brown–orange–red and has a wider range in composition,. For example, titanite
31
32 413 reported in Garber et al. (2017)—which might be considered typical for granitic rocks—has 0.5–
33
34 414 2 wt.% each of Al, Fe, and F (2–3x higher than the titanite used in experiments) as well as 0.2–
35
36 415 7.1 wt.% trace elements (measured by LASS; median = 1.3 wt.%). In the calc-silicate samples
37
38 416 12D and 21B of this study, non-CaTiSiO₅ substituents comprise 3.9–6.0 and 8.9–13.1 wt%,
39
40 417 respectively (Table 1; Online Resource 5). These points emphasize that most natural titanite
41
42 418 grains have more complex solid solutions (commonly ≥10–20 mol% non-CaTiSiO₅ end-
43
44 419 members) than the titanite used in experimental diffusion studies (6 mol% non-CaTiSiO₅ end-
45
46 420 members; Cherniak, 1993, 1995). Most of these minor and trace elements are accommodated in
47
48 421 titanite by multiple coupled substitutions that may not have operated in experiments with purer
49
50 422 titanite.

51
52 423 The possible importance of coupled versus uncoupled diffusion in titanite, as well as the
53
54 424 complexity of individual diffusion mechanisms is illustrated in part by the experiments of
55
56 425 Cherniak (1995) on Sr and Nd diffusion. Cherniak found that Nd diffusion in air was ~1 order of
57
58 426 magnitude faster than Nd diffusion buffered at FMQ. The activation energies of diffusion were
59
60 427 lower in air than at FMQ, indicating that the diffusion mechanism was different. Nd diffusion
61
62 428 was coupled to Al diffusion (one-to-one) in experiments conducted at FMQ, but showed no

4 429 coupling to Al (and Al showed no evidence of diffusion) in experiments conducted in air. The
5
6 430 coupling of Nd to Al at FMQ can be explained by the reaction $\text{Nd}^{3+} + \text{Al}^{3+} \leftrightarrow \text{Ca}^{2+} + \text{Ti}^{4+}$, but
7
8 431 the mechanism for the apparently uncoupled diffusion in air is unclear. Cherniak suggested that
9
10 432 it might be related to the presence of defects (a faster diffusion pathway) created by the oxidation
11
12 433 of Fe (the samples changed from green to red when annealed in air prior to experiments), or by
13
14 434 coupled substitution with anions on the volatile site (O, OH, F, Cl), although she did not find
15
16 435 appreciable differences in O or F contents among untreated, annealed-in-air, or annealed-at-FMQ
17
18 436 samples. The apparently uncoupled Nd diffusion in air (faster than at FMQ) was found to have
19
20 437 the same rate as Sr diffusion, which was also interpreted to be uncoupled ($\text{Sr}^{2+} \leftrightarrow \text{Ca}^{2+}$) and did
21
22 438 not have different diffusion rates at different $f\text{O}_2$. These experiments show that order-of-
23
24 439 magnitude differences in elemental diffusivities (of Nd and Al) can result from differences in
25
26 440 how elements are coupled in the crystal lattice and, possibly, differences in ambient conditions
27
28 441 (in this case, $f\text{O}_2$).

28 442 In experiments on Nb and Ta diffusivity (Cherniak, 2015), the length scales of Nb and Ta
29
30 443 diffusion were found to be identical to the length scales of Al diffusion, although the molar
31
32 444 proportions of Al were not sufficient to charge balance the amount of Nb–Ta present, suggesting
33
34 445 that other elements (Fe^{3+} , Na^+ , F^-) must have been involved. Even in the relatively simple titanite
35
36 446 used in experiments, diffusion of a single element may require exchange of other elements in the
37
38 447 crystal lattice. The correlations between Al and Nd–Nb–Ta diffusion suggest that trace-element
39
40 448 diffusivities and Al (and Fe^{3+}) diffusivity are fundamentally linked, such that movement of any
41
42 449 of these elements will be partially limited by the mobility of other elements. This interpretation is
43
44 450 supported by the similarities among calculated diffusivities for Al, Nb, and Ce (a REE, like Nd)
45
46 451 in this study.

46 452 The complexity of cation substitution in titanite is also highlighted by Prowatke and
47
48 453 Klemme's (2005) experimental study of trace-element partitioning between titanite and silicate
49
50 454 melt. Prowatke and Klemme found that total REE–Nb–Ta partitioning into titanite was
51
52 455 correlated with titanite Al content, but that Al content was independent of REE–Nb–Ta content.
53
54 456 The correlation between Al and total REE–Nb–Ta concentrations was nonlinear. They concluded
55
56 457 that titanite–melt trace-element partitioning was affected more by trace-element coordination in
57
58 458 the melt than by changes in crystal structure caused by changes in titanite composition. More
59
60 459 importantly for this discussion, Prowatke and Klemme concluded that the substitution of REE–

4
5 460 Ta–Nb into titanite may have involved vacancies ($4\text{Nb}^{5+} + \square \leftrightarrow 5\text{Ti}^{4+}$, $2\text{REE}^{3+} + \square \leftrightarrow 3\text{Ca}^{2+}$),
6
7 461 in addition to the aforementioned coupled substitutions involving Al.

8
9 462 Although Prowatke and Klemme concluded that total REE partitioning was not a function of
10
11 463 Al content, they did recognize changes in the physical properties of the titanite crystal lattice as a
12
13 464 function of Al content. With increasing titanite Al content, their REE profiles exhibited more-
14
15 465 pronounced MREE enrichment (higher Gd relative to La and Lu). Lattice strain models of REE
16
17 466 substitution into the Ca site suggested an increase in the apparent Young's modulus by a factor
18
19 467 of 2.3 for an increase in Al_2O_3 of 0.13 to 0.69 wt.%; natural titanite commonly exhibits much
20
21 468 higher concentrations (e.g. this study; Franz and Spear, 1985; Garber et al., 2017). Garber et al.
22
23 469 (2017) noted the same correlation between REE concavity and Al content in Norwegian titanite,
24
25 470 and interpreted this to reflect decreases in the Ca–O and [Ti,Al]–O bond lengths and unit-cell
26
27 471 volume as a function of Al \leftrightarrow Ti substitution (Oberti et al., 1991).

27 472 To summarize, most natural titanite is a more-complex solid solution than titanite used in
28
29 473 diffusion experiments. Non- CaTiSiO_5 substituents in titanite commonly comprise ≥ 5 –10 wt.%
30
31 474 (≥ 10 –20 mol% non- CaTiSiO_5 end members). The substitution of Al is most prominent and has
32
33 475 been studied in the most detail. Incorporation of Al has been shown to correspond to changes in
34
35 476 the size and elasticity of the titanite lattice. Although speculative, these changes in composition
36
37 477 and crystal structure might correspond to changes in elemental diffusivities, as has been shown
38
39 478 for interdiffusion in metal alloys (Porter and Easterling, 1990) and predicted for O diffusion in
40
41 479 silicates (Zheng and Fu, 1998). Most substituents enter the titanite lattice through multiple
42
43 480 coupled substitution mechanisms, such that none of the substituents likely diffuse independently
44
45 481 of the others. The rates of even relatively simple diffusion mechanisms, like $\text{Zr}^{4+} \leftrightarrow \text{Ti}^{4+}$, might
46
47 482 be limited by the extent to which each of these elements is coupled to other elements in the
48
49 483 titanite lattice (such as Al^{3+} , which occupies the same site, but is coupled to substituents on the
50
51 484 Ca- and O-sites). Another parameter than might influence elemental diffusivities in a complex
52
53 485 solid solution like titanite are the abundance of vacancies; however, assessment of the role of
54
55 486 vacancies on cation diffusion is beyond the capabilities of the data presented in this study.

56 488 CONCLUSIONS

57
58 489 Elemental diffusivities in titanite were estimated from the length scales of compositional and
59
60 490 isotopic heterogeneity in granulite-facies titanite from southern Madagascar (Fig. 10; Table 2).

4 491 The calculated Pb diffusivities are similar to the experimental data for Sr (Cherniak, 1995),
5
6 492 implying that most titanite U–Pb dates will be preserved through temperatures as high as 850°C
7
8 493 and should not be interpreted as cooling ages unless grain-scale evidence for volume diffusion
9
10 494 can be documented; strategies for differentiating diffusion, growth, and other mechanisms of
11
12 495 recrystallization (*sensu lato*) based on U–Pb zoning have previously been outlined by Stearns et
13
14 496 al. (2015) and Smye et al. (2018). The elements Al, Fe, Nb, Zr, and Ce diffuse slower than Pb
15
16 497 and reflect the conditions of titanite crystallization in all but the highest grade rocks (>850°C).
17
18 498 Although the calculations in this study are subject to terrane-scale geological uncertainty, they
19
20 499 provide a quantitative framework, consistent with previous semi-quantitative empirical studies,
21
22 500 to assess and refine understanding of titanite petrochronology and elemental diffusion. It is
23
24 501 hypothesized that differences between empirical and experimental diffusivities may be related to
25
26 502 physical and chemical differences between most natural titanite and near-end-member CaTiSiO₅
27
28 503 titanite used in experiments.

30 **Acknowledgements**

31
32 506 This work was funded by NSF EAR-1348003, NSF EAR-1551054, and the University of
33
34 507 California, Santa Barbara. Andrew Smye provided helpful feedback on an earlier version of this
35
36 508 work. Editor Daniela Rubatto, reviewer James Van Orman, and an anonymous reviewer
37
38 509 provided constructive feedback and suggestions on the content and broader organization of ideas.
39
40
41
42
43
44
45
46
47
48
49
50
51
52
53
54
55
56
57
58
59
60
61

4 511 **Electronic Supplementary Material**

5	6	7
8	File	Content
9	ESM_1–4.docx	Online Resource 1. Experimental estimates of elemental diffusivity 10 in titanite 11 12 Online Resource 2. Empirical estimates of elemental diffusivity in 13 titanite 14 15 Online Resource 3. Methods: Laser-ablation split-stream inductively 16 coupled plasma mass spectrometry (LASS) depth profiles 17 18 Online Resource 4. Methods: EPMA spot analyses 19 20 21
22	ESM_5–10.xlsx	Online Resource 5. EPMA spot analyses 23 24 Online Resource 6. Comparison of quantified EPMA maps and spot 25 analyses in titanite 21B 26 27 Online Resource 7. LASS depth profiles from titanite 12D 28 29 Online Resource 8. EPMA profiles from titanite 12D 30 31 Online Resource 9. Pb-isotope analyses of clinopyroxene 32 33 Online Resource 10. LASS spot data for titanite 21B 34 35 Online Resource 11. EPMA profiles ttn 21B 36

37 512

38 513

39
40
41
42
43
44
45
46
47
48
49
50
51
52
53
54
55
56
57
58
59
60
61

References

- Boger, S.D., Hirdes, W., Ferreira, C.A.M., Jenett, T., Dallwig, R., Fanning, C.M., 2015. The 580–520 Ma Gondwana suture of Madagascar and its continuation into Antarctica and Africa. *Gondwana Res.* 28, 1048–1060. doi:10.1016/j.gr.2014.08.017
- Boger, S.D., White, R.W., Schulte, B., 2012. The importance of iron speciation (Fe²⁺/Fe³⁺) in determining mineral assemblages: an example from the high-grade aluminous metapelites of southeastern Madagascar. *J. Metamorph. Geol.* 30, 997–1018. doi:10.1111/jmg.12001
- Bonamici, C.E., Fanning, C.M., Kozdon, R., Fournelle, J.H., Valley, J.W., 2015. Combined oxygen-isotope and U-Pb zoning studies of titanite: New criteria for age preservation. *Chem. Geol.* 398, 70–84. doi:10.1016/j.chemgeo.2015.02.002
- Castelli, D., Rubatto, D., 2002. Stability of Al- and F-rich titanite in metacarbonate: Petrologic and isotopic constraints from a polymetamorphic eclogitic marble of the internal Sesia zone (Western Alps). *Contrib. to Mineral. Petrol.* 142, 627–639. doi:10.1007/s00410-001-0317-6
- Chambers, J.A., Kohn, M.J., 2012. Titanium in muscovite, biotite, and hornblende: Modeling, thermometry, and rutile activities of metapelites and amphibolites. *Am. Mineral.* 97, 543–555. doi:10.2138/am.2012.3890
- Cherniak, D.J., 2015. Nb and Ta diffusion in titanite. *Chem. Geol.* 413, 44–50. doi:10.1016/j.chemgeo.2015.08.010
- Cherniak, D.J., 2006. Zr diffusion in titanite. *Contrib. to Mineral. Petrol.* 152, 639–647. doi:10.1007/s00410-006-0133-0
- Cherniak, D.J., 1995. Sr and Nd diffusion in titanite. *Chem. Geol.* 125, 219–232. doi:10.1016/0009-2541(95)00074-V
- Cherniak, D.J., 1993. Lead diffusion in titanite and preliminary results on the effects of radiation damage on Pb transport. *Chem. Geol.* 110, 177–194. doi:10.1016/0009-2541(93)90253-F
- Collins, A.S., Kinny, P.D., Razakamanana, T., 2012. Depositional age, provenance and metamorphic age of metasedimentary rocks from southern Madagascar. *Gondwana Res.* 21, 353–361. doi:10.1016/j.gr.2010.12.006
- Corfu, F., 1996. Multistage zircon and titanite growth and inheritance in an Archean gneiss complex, Winnipeg River Subprovince, Ontario. *Earth Planet. Sci. Lett.* 141, 175–186. doi:10.1016/0012-821X(96)00064-7
- Donovan, J.J., Singer, J.W., Armstrong, J.T., 2016. A new EPMA method for fast trace element analysis in simple matrices. *Am. Mineral.* 101, 1839–1853. doi:10.2138/am-2016-5628
- Fitzsimons, I.C.W., 2016. Pan-African granulites of Madagascar and southern India: Gondwana assembly and parallels with modern Tibet. *J. Mineral. Petrol. Sci.* 111, 73–88. doi:10.2465/jmps.151117
- Franz, G., Spear, F.S., 1985. Aluminous titanite (sphene) from the Eclogite Zone, south-central Tauern Window, Austria. *Chem. Geol.* 50, 33–46. doi:10.1016/0009-2541(85)90110-X
- Frost, B.R., Chamberlain, K.R., Schumacher, J.C., 2000. Sphene (titanite): phase relations and role as a geochronometer. *Chem. Geol.* 172, 131–148. doi:10.1016/S0009-2541(00)00240-0
- Ganne, J., Nédélec, a., Grégoire, V., Gouy, S., de Parseval, P., 2014. Tracking Late-Pan-African fluid composition evolution in the ductile crust of Madagascar: Insight from phase relation modelling of retrogressed gneisses (province of Fianarantsoa). *J. African Earth Sci.* 94, 100–110. doi:10.1016/j.jafrearsci.2013.10.004
- Gao, X.-Y., Zheng, Y.-F., Chen, Y.-X., Guo, J., 2012. Geochemical and U–Pb age constraints on the occurrence of polygenetic titanites in UHP metagranite in the Dabie orogen. *Lithos* 136–139, 93–108. doi:10.1016/j.lithos.2011.03.020

- 4 560 Garber, J.M., Hacker, B.R., Kylander-Clark, A.R.C., Stearns, M.A., Seward, G., 2017. Controls
5 561 on trace element uptake in metamorphic titanite: Implications for petrochronology. *J. Petrol.*
6 562 58, 1031–1057. doi:10.1093/petrology/egx046
- 8 563 Ghent, E.D., Stout, M.Z., 1984. TiO₂ activity in metamorphosed pelitic and basic rocks:
9 564 principles and applications to metamorphism in southeastern Canadian Cordillera. *Contrib.*
10 565 *to Mineral. Petrol.* 86, 248–255. doi:10.1007/BF00373670
- 12 566 Grégoire, V., Nédélec, A., Monié, P., Montel, J.-M., Ganne, J., Ralison, B., 2009. Structural
13 567 reworking and heat transfer related to the late-Panafrican Angavo shear zone of
14 568 Madagascar. *Tectonophysics* 477, 197–216. doi:10.1016/j.tecto.2009.03.009
- 15 569 Hayden, L.A., Watson, E.B., Wark, D.A., 2008. A thermobarometer for sphene (titanite).
16 570 *Contrib. to Mineral. Petrol.* 155, 529–540. doi:10.1007/s00410-007-0256-y
- 18 571 Holder, R.M., Hacker, B.R., 2019. Fluid-driven resetting of titanite following ultrahigh-
19 572 temperature metamorphism in southern Madagascar. *Chem. Geol.* 504, 38–52.
20 573 doi:10.1016/j.chemgeo.2018.11.017
- 21 574 Holder, R.M., Hacker, B.R., Horton, F., Rakotondrazafy, A.F.M., 2018a. Ultrahigh-temperature
22 575 osumilite gneisses in southern Madagascar record combined heat advection and high rates
23 576 of radiogenic heat production in a long-lived high- T orogen. *J. Metamorph. Geol.* 36, 855–
24 577 880. doi:10.1111/jmg.12316
- 26 578 Holder, R.M., Sharp, Z.D., Hacker, B.R., 2018b. LinT, a simplified approach to oxygen-isotope
27 579 thermometry and speedometry of high-grade rocks: An example from ultrahigh-temperature
28 580 gneisses of southern Madagascar. *Geology*. doi:10.1130/G40207.1
- 30 581 Horton, F., Hacker, B.R., Kylander-Clark, A.R.C., Holder, R.M., Jöns, N., 2016. Focused
31 582 radiogenic heating of middle crust caused ultrahigh temperatures in southern Madagascar.
32 583 *Tectonics* 35, 293–314. doi:10.1002/2015TC004040
- 34 584 Jöns, N., Schenk, V., 2011. The ultrahigh temperature granulites of southern Madagascar in a
35 585 polymetamorphic context: implications for the amalgamation of the Gondwana
36 586 supercontinent. *Eur. J. Mineral.* 23, 127–156. doi:10.1127/0935-1221/2011/0023-2087
- 37 587 Kirkland, C.L., Spaggiari, C. V., Johnson, T.E., Smithies, R.H., Danišík, M., Evans, N., Wingate,
38 588 M.T.D., Clark, C., Spencer, C., Mikucki, E., McDonald, B.J., 2016. Grain size matters:
39 589 Implications for element and isotopic mobility in titanite. *Precambrian Res.* 278, 283–302.
40 590 doi:10.1016/j.precamres.2016.03.002
- 42 591 Kohn, M.J., 2017. Titanite Petrochronology. *Rev. Mineral. Geochemistry* 83.
43 592 doi:10.2138/rmg.2017.83.13
- 44 593 Kohn, M.J., Corrie, S.L., 2011. Preserved Zr-temperatures and U–Pb ages in high-grade
45 594 metamorphic titanite: Evidence for a static hot channel in the Himalayan orogen. *Earth*
46 595 *Planet. Sci. Lett.* 311, 136–143. doi:10.1016/j.epsl.2011.09.008
- 48 596 Kohn, M.J., Penniston-Dorland, S.C., Ferreira, J.C.S., 2016. Implications of near-rim
49 597 compositional zoning in rutile for geothermometry, geospeedometry, and trace element
50 598 equilibration. *Contrib. to Mineral. Petrol.* doi:10.1007/s00410-016-1285-1
- 52 599 Košler, J., Sláma, J., Belousova, E., Corfu, F., Gehrels, G.E., Gerdes, A., Horstwood, M.S.A.,
53 600 Sircombe, K.N., Sylvester, P.J., Tiepolo, M., Whitehouse, M.J., Woodhead, J.D., 2013. U-
54 601 Pb detrital zircon analysis - results of an inter-laboratory comparison. *Geostand.*
55 602 *Geoanalytical Res.* 37, 243–259. doi:10.1111/j.1751-908X.2013.00245.x
- 57 603 Kylander-Clark, A.R.C., 2017. Petrochronology by Laser-Ablation Inductively Coupled Plasma
58 604 Mass Spectrometry. *Rev. Mineral. Geochemistry* 83, 183–196. doi:10.2138/rmg.2017.83.6
- 59 605 Kylander-Clark, A.R.C., Hacker, B.R., Cottle, J.M., 2013. Laser-ablation split-stream ICP
60
61

- 4 606 petrochronology. *Chem. Geol.* 345, 99–112. doi:10.1016/j.chemgeo.2013.02.019
- 5 607 Kylander-Clark, A.R.C., Hacker, B.R., Mattinson, J.M., 2008. Slow exhumation of UHP
- 6 608 terranes: Titanite and rutile ages of the Western Gneiss Region, Norway. *Earth Planet. Sci.*
- 7 609 *Lett.* 272, 531–540. doi:10.1016/j.epsl.2008.05.019
- 8 610 Marsh, J.H., Smye, A.J., 2017. U-Pb systematics and trace element characteristics in titanite
- 9 611 from a high-pressure mafic granulite. *Chem. Geol.* 466, 403–416.
- 10 612 doi:10.1016/j.chemgeo.2017.06.029
- 11 613 Mattinson, J.M., 1978. Age, origin, and thermal histories of some plutonic rocks from the
- 12 614 Salinian block of California. *Contrib. to Mineral. Petrol.* 67, 233–245.
- 13 615 doi:10.1007/BF00381451
- 14 616 Mezger, K., Essene, E.J., van der Pluijm, B.A., Halliday, A.N., 1993. U-Pb geochronology of the
- 15 617 Grenville Orogen of Ontario and New York: constraints on ancient crustal tectonics.
- 16 618 *Contrib. to Mineral. Petrol.* 114, 13–26. doi:10.1007/BF00307862
- 17 619 Mezger, K., Rawnsley, C.M., Bohlen, S.R., Hanson, G.N., 1991. U-Pb Garnet, Sphene,
- 18 620 Monazite, and Rutile Ages: Implications for the Duration of High-Grade Metamorphism
- 19 621 and Cooling Histories, Adirondack Mts., New York. *J. Geol.* 99, 415–428.
- 20 622 doi:10.1086/629503
- 21 623 Montel, J.-M., Razafimahatratra, D., de Parseval, P., Poitrasson, F., Moine, B., Seydoux-
- 22 624 Guillaume, A.-M., Pik, R., Arnaud, N., Gibert, F., 2018. The giant monazite crystals from
- 23 625 Manangotry (Madagascar). *Chem. Geol.* 484, 36–50. doi:10.1016/j.chemgeo.2017.10.034
- 24 626 Mottram, C.M., Cottle, J., Kylander-Clark, A., 2018. Campaign-style U-Pb titanite
- 25 627 petrochronology; along-strike variations in timing of metamorphism in the Himalayan
- 26 628 Metamorphic Core. *Geosci. Front.* doi:10.1016/j.gsf.2018.09.007
- 27 629 Oberti, R., Smith, D.C., Rossi, G., Caucia, F., 1991. The crystal-chemistry of high-aluminium
- 28 630 titanites. *Eur. J. Mineral.* 3, 777–792. doi:10.1127/ejm/3/5/0777
- 29 631 Olierook, H.K.H., Taylor, R.J.M., Erickson, T.M., Clark, C., Reddy, S.M., Kirkland, C.L., Jahn,
- 30 632 I., Barham, M., 2018. Unravelling complex geologic histories using U–Pb and trace element
- 31 633 systematics of titanite. *Chem. Geol.* 0–1. doi:10.1016/j.chemgeo.2018.11.004
- 32 634 Paquette, J.-L., Nédélec, A., Moine, B., Rakotondrazafy, A.F.M., 1994. U-Pb, Single Zircon Pb-
- 33 635 Evaporation, and Sm-Nd Isotopic Study of a Granulite Domain in SE Madagascar. *J. Geol.*
- 34 636 102, 523–538. doi:10.1086/629696
- 35 637 Pidgeon, R.T., Bosch, D., Bruguier, O., 1996. Inherited zircon and titanite U–Pb systems in an
- 36 638 Archean syenite from southwestern Australia: implications for U–Pb stability of titanite.
- 37 639 *Earth Planet. Sci. Lett.* 141, 187–198. doi:10.1016/0012-821X(95)00237-7
- 38 640 Porter, D.A., Easterling, K.E., 1990. Diffusion, in: *Phase Transformations in Metals and Alloys.*
- 39 641 Chapman and Hall, New York, pp. 60–109.
- 40 642 Prowatke, S., Klemme, S., 2005. Effect of melt composition on the partitioning of trace elements
- 41 643 between titanite and silicate melt. *Geochim. Cosmochim. Acta* 69, 695–709.
- 42 644 doi:10.1016/j.gca.2004.06.037
- 43 645 Rakotondrazafy, A.F.M., Moine, B., Cuney, M., 1996. Mode of formation of hibonite
- 44 646 (CaAl₁₂O₁₉) within the U-Th skarns from the granulites of S-E Madagascar. *Contrib. to*
- 45 647 *Mineral. Petrol.* 123, 190–201. doi:10.1007/s004100050150
- 46 648 Rubatto, D., Hermann, J., 2001. Exhumation as fast as subduction? *Geology* 29, 3–6.
- 47 649 doi:10.1130/0091-7613(2001)029<0003:EAFAS>2.0.CO
- 48 650 Schärer, U., Zhang, L.-S., Tapponnier, P., 1994. Duration of strike-slip movements in large shear
- 49 651 zones: The Red River belt, China. *Earth Planet. Sci. Lett.* doi:10.1016/0012-
- 50
- 51
- 52
- 53
- 54
- 55
- 56
- 57
- 58
- 59
- 60
- 61

- 4 652 821X(94)90119-8
- 5 653 Scott, D.J., St-Onge, M.R., 1995. Constraints on Pb closure temperature in titanite based on
- 6 654 rocks from the Ungava orogen, Canada: Implications for U-Pb geochronology and P-T-t
- 7 655 path determinations. *Geology* 23, 1123–1126.
- 8 656 Smye, A.J., Marsh, J.H., Vermeesch, P., Garber, J.M., Stockli, D.F., 2018. Applications and
- 9 657 limitations of U-Pb thermochronology to middle and lower crustal thermal histories. *Chem.*
- 10 658 *Geol.* 494, 1–18. doi:10.1016/j.chemgeo.2018.07.003
- 11 659 Spear, F.S., Parrish, R.R., 1996. Petrology and cooling rates of the Valhalla Complex, British
- 12 660 Columbia, Canada. *J. Petrol.* 37, 733–765.
- 13 661 Spencer, K.J., Hacker, B.R., Kylander-Clark, A.R.C., Andersen, T.B., Cottle, J.M., Stearns,
- 14 662 M.A., Poletti, J.E., Seward, G.G.E., 2013. Campaign-style titanite U–Pb dating by laser-
- 15 663 ablation ICP: Implications for crustal flow, phase transformations and titanite closure.
- 16 664 *Chem. Geol.* 341, 84–101. doi:10.1016/j.chemgeo.2012.11.012
- 17 665 Stearns, M.A., Cottle, J.M., Hacker, B.R., Kylander-Clark, A.R.C., 2016. Extracting thermal
- 18 666 histories from the near-rim zoning in titanite using coupled U-Pb and trace-element depth
- 19 667 profiles by single-shot laser-ablation split stream (SS-LASS) ICP-MS. *Chem. Geol.* 422,
- 20 668 13–24. doi:10.1016/j.chemgeo.2015.12.011
- 21 669 Stearns, M.A., Hacker, B.R., Ratschbacher, L., Rutte, D., Kylander-Clark, A.R.C., 2015. Titanite
- 22 670 petrochronology of the Pamir gneiss domes: Implications for middle to deep crust
- 23 671 exhumation and titanite closure to Pb and Zr diffusion. *Tectonics* 34, 784–802.
- 24 672 doi:10.1002/2014TC003774
- 25 673 Tucker, R.D., Krogh, T.E., Ross, R.J., Williams, S.H., 1990. Time-scale calibration by high-
- 26 674 precision U–Pb zircon dating of interstratified volcanic ashes in the Ordovician and Lower
- 27 675 Silurian stratotypes of Britain. *Earth Planet. Sci. Lett.* 100, 51–58. doi:10.1016/0012-
- 28 676 821X(90)90175-W
- 29 677 Tucker, R.D., Råheim, A., Krogh, T.E., Corfu, F., 1987. Uranium-lead zircon and titanite ages
- 30 678 from the northern portion of the Western Gneiss Region, south-central Norway. *Earth*
- 31 679 *Planet. Sci. Lett.* 81, 203–211. doi:10.1016/0012-821X(87)90156-7
- 32 680 Tucker, R.D., Robinson, P., Solli, A., Gee, D.G., Thorsnes, T., Krogh, T.E., Nordgulen, Ø.,
- 33 681 Bickford, M.E., 2004. Thrusting and extension in the Scandian hinterland, Norway: New U-
- 34 682 Pb ages and tectonostratigraphic evidence. *Am. J. Sci.* 304, 477–532.
- 35 683 doi:10.2475/03.2011.01
- 36 684 Tucker, R.D., Roig, J.-Y., Delor, C., Amelin, Y., Goncalves, P., Rabarimanana, M.H., Ralison,
- 37 685 a. V., Belcher, R.W., 2011. Neoproterozoic extension in the Greater Dharwar Craton: a
- 38 686 reevaluation of the “Betsimisaraka suture” in Madagascar. *Can. J. Earth Sci.* 48, 389–417.
- 39 687 doi:10.1139/E10-034
- 40 688 Tucker, R.D., Roig, J.Y., Moine, B., Delor, C., Peters, S.G., 2014. A geological synthesis of the
- 41 689 Precambrian shield in Madagascar. *J. African Earth Sci.* 94, 9–30.
- 42 690 doi:10.1016/j.jafrearsci.2014.02.001
- 43 691 Verts, L.A., Chamberlain, K.R., Frost, C.D., 1996. U-Pb sphene dating of metamorphism: the
- 44 692 importance of sphene growth in the contact aureole of the Red Mountain pluton, Laramie
- 45 693 Mountains, Wyoming. *Contrib. to Mineral. Petrol.* 125, 186–199.
- 46 694 doi:10.1007/s004100050215
- 47 695 Walters, J.B., Kohn, M.J., 2017. Protracted thrusting followed by late rapid cooling of the
- 48 696 Greater Himalayan Sequence, Annapurna Himalaya, Central Nepal: Insights from titanite
- 49 697 petrochronology. *J. Metamorph. Geol.* 35, 897–917. doi:10.1111/jmg.12260
- 50
- 51
- 52
- 53
- 54
- 55
- 56
- 57
- 58
- 59
- 60
- 61

4 698 Watson, E.B., Cherniak, D.J., 2015. Quantitative cooling histories from stranded diffusion
5 699 profiles. *Contrib. to Mineral. Petrol.* 169, 1–14. doi:10.1007/s00410-015-1153-4
6 700 Zhang, L.-S., Schärer, U., 1996. Inherited Pb components in magmatic titanite and their
7 701 consequence for the interpretation of U–Pb ages. *Earth Planet. Sci. Lett.* 138, 57–65.
8 702 Zhang, X.Y., Cherniak, D.J., Watson, E.B., 2006. Oxygen diffusion in titanite: Lattice diffusion
9 703 and fast-path diffusion in single crystals. *Chem. Geol.* 235, 105–123.
10 704 doi:10.1016/j.chemgeo.2006.06.005
11 705 Zheng, Y.F., Fu, B., 1998. Estimation of oxygen diffusivity from anion porosity in minerals.
12 706 *Geochem. J.* 32, 71–89. doi:10.2343/geochemj.32.71
13 707
14 708
15
16
17
18
19
20
21
22
23
24
25
26
27
28
29
30
31
32
33
34
35
36
37
38
39
40
41
42
43
44
45
46
47
48
49
50
51
52
53
54
55
56
57
58
59
60
61

4 709 **Figure Captions**

5 710
6 711 **Fig. 1** (a) Simplified geological map of the tectonometamorphic domains of southern
7 712 Madagascar showing the locations of samples used in this study and diagnostic high-temperature
8 713 mineral assemblages modified after Holder and Hacker (2019; the assemblage spinel–quartz is
9 714 also known throughout the Anosyen Domain and eastern Androyen Domain). (b) Location of
10 715 study area in Madagascar. (c) Photograph of a typical calc-silicate gneiss with large titanite
11 716 grains near Tranomaro: 2 cm chisel for scale. (c) Thin section (2x4.5 cm) of typical calc-silicate
12 717 gneiss. Mineral abbreviations after Kretz (1983)
13 718

14 719 **Fig. 2** Near-rim compositional and isotopic zoning in titanite 12D was measured by LASS depth
15 720 profiling of a crystal face followed by sectioning the grain perpendicular to the analyzed crystal
16 721 face and mapping the sectioned plane by EPMA. Results of these analyses are shown in Figs. 4–
17 722 6. Elemental diffusivities calculated from near-rim zoning are shown in Table 2 and Fig. 10
18 723

19 724 **Fig. 3** Comparison of elemental concentrations in titanite 21B calculated from individual pixels
20 725 of a quantified EPMA map and traditional EPMA spot analyses on the same location,
21 726 demonstrating the accuracy of the map quantification method described in the text. The plotted
22 727 data are available in Online Resource 6
23 728

24 729 **Fig. 4** Near-rim concentration gradients of ^{206}Pb (a), ^{207}Pb (b), ^{208}Pb (c), Th (d), U (e), and Zr (f)
25 730 as well as isotope-ratio gradients of $^{206}\text{Pb}/^{238}\text{U}$ (g), $^{207}\text{Pb}/^{235}\text{U}$ (h), and $^{207}\text{Pb}/^{206}\text{Pb}$ (i) measured by
26 731 LASS in titanite 12D. Points are the individual data from each of four depth profiles measured
27 732 on the same crystal face. The line is the average of all four profiles. The precision of each datum
28 733 and the 2 σ uncertainty of the average profile for each isotope and ratio are presented in the
29 734 corresponding panels. ^{206}Pb and ^{207}Pb profiles mimic U and ^{208}Pb mimics Th, as expected for a
30 735 system that has remained closed since 500 Ma. Decreases in Pb/U isotope ratios toward the grain
31 736 rim could reflect protracted growth or diffusional Pb loss. Diffusional Pb loss is the favored
32 737 interpretation for these data for reasons outlined in the text. Fig. 5 shows the common-Pb
33 738 corrected U–Pb date profile and corresponding concordia diagram
34 739

35 740 **Fig. 5** (a) Common-Pb-corrected $^{206}\text{Pb}/^{238}\text{U}$ date profile for LASS analyses of the crystal face of
36 741 titanite 12D and (b) corresponding concordia diagram showing each datum of the averaged
37 742 profile colored by depth from the crystal face. Data in (a) were corrected using the $^{207}\text{Pb}/^{206}\text{Pb}$
38 743 composition of clinopyroxene in the same rock (so-called ^{207}Pb -corrected $^{206}\text{Pb}/^{238}\text{U}$ dates or
39 744 Tera–Wasserburg intercept dates anchored to $^{207}\text{Pb}/^{206}\text{Pb}$). The abrupt decrease in U–Pb date in
40 745 the outermost 5 μm is interpreted to reflect diffusional loss of Pb. See text for discussion
41 746

42 747 **Fig. 6** (a) Elemental concentration maps perpendicular to titanite 12D crystal face. Two of the
43 748 four LASS depth profiles (Figs. 5 and 6) are partially exposed. Irregularities in the shape of the
44 749 laser pits are due to damage accrued during sectioning and polishing: qualitatively visible by the
45 750 accumulation of polishing medium along fractions and the edges of the pits (Al and Fe maps).
46 751 (b) Elemental concentration profiles extracted by swath transect of the area between the two
47 752 LASS pits. Zr, Al, and Fe decrease monotonically toward the crystal face and show no evidence
48 753 for near-rim diffusion. Possible diffusive influx of Nb and Ce are inferred from increases in their
49 754 concentrations in the outermost 6 and 20 μm , respectively; however, the absence of any apparent
50 755
51
52
53
54
55
56
57
58
59
60
61

4 755 diffusion profiles in Zr, Al, or Fe suggest the Nb and Ce profiles might be growth zoning.
5 756 Maximum elemental diffusivities inferred from these compositional profiles are shown in Table
6 757 2 and Fig. 10
7 758

9 759 **Fig. 7** (a) LASS U–Pb map and EPMA Al, Fe, Zr, Nb, and Ce maps for titanite 21B. The LASS
10 760 U–Pb map is shown in more detail in Fig. 8. Steep compositional gradients in the EPMA maps,
11 761 marked with stars, were modeled as diffusively relaxed compositional steps to estimate
12 762 elemental diffusivities in titanite (Figs. 9 and 10). (b) Higher magnification images of steep
13 763 compositional gradients in Zr used to calculate elemental diffusivities. The map resolution is 10
14 764 μm
15 765

17 766 **Fig. 8** Map of LASS U–Pb dates in titanite 21B with. Surrounding minerals are labeled with the
18 767 symbology of Kretz (1983). Dates are $^{206}\text{Pb}/^{238}\text{U}$ dates corrected for common Pb using the
19 768 $^{207}\text{Pb}/^{206}\text{Pb}$ composition of clinopyroxene from the same thin section. Dates correspond to the
20 769 timing of peak metamorphism (550 ± 11 Ma; Holder et al., 2018) and subsequent cooling. The
21 770 preservation of U–Pb dates corresponding to the timing of peak or near-peak temperature
22 771 metamorphism was used to estimate Pb diffusivity in titanite (Table 2; Fig. 10)
23 772

24 773 **Fig. 9** Elemental concentration profiles across the steep compositional gradients shown in Fig. 7
25 774 and best-fit error functions to each profile (black lines). Error bars are 2se. Elemental
26 775 diffusivities were calculated from these profiles using an independently constrained thermal
27 776 history (Holder et al., 2018; Montel et al., 2018) and the equations of Watson and Cherniak
28 777 (2015). Calculated diffusivities are shown in Table 2 and Figure 10.
29 778

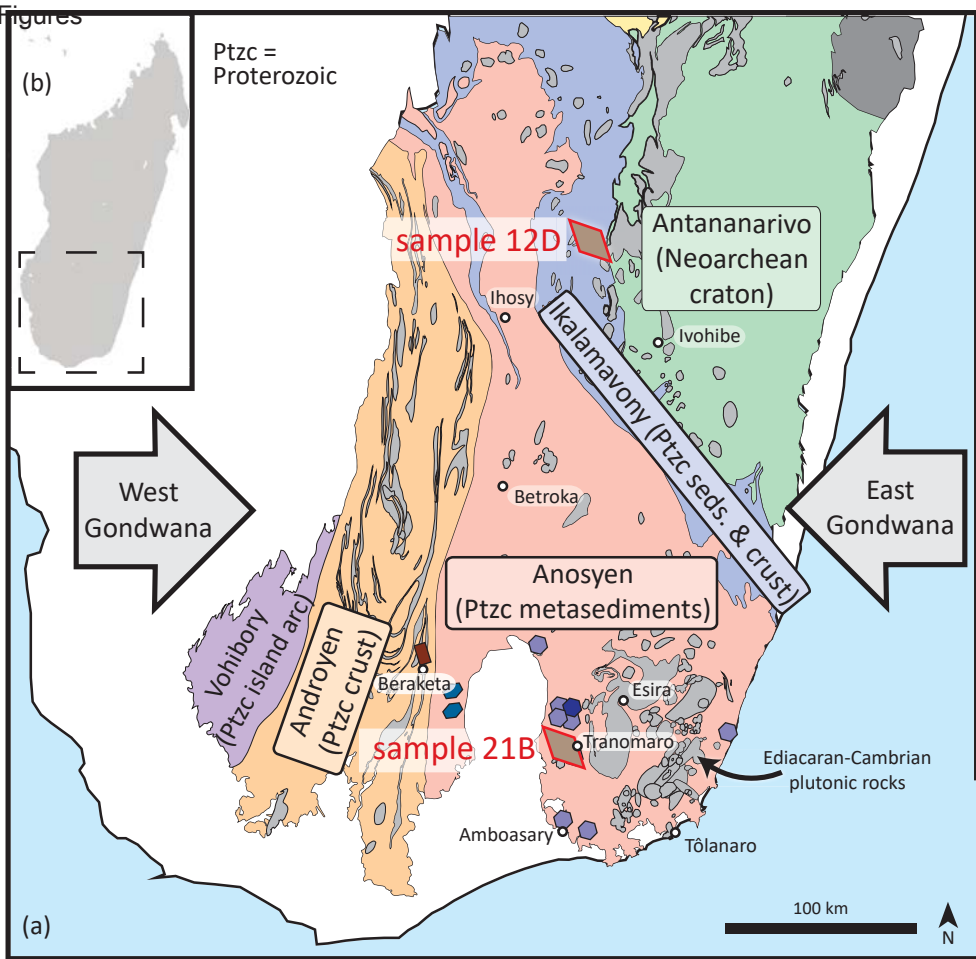
30 779 **Fig. 10** Calculated elemental diffusivities from this study compared to experimental data. (a)
31 780 Calculated Pb diffusivities from rocks are similar to experimental Sr diffusivity, but slower than
32 781 experimental Pb diffusivity as hypothesized by Kohn (2017). For rocks that reached peak
33 782 temperatures $\leq 850^\circ\text{C}$, titanite U–Pb dates likely reflect the timing of titanite (re)crystallization,
34 783 rather than a cooling age. (b–f) Other cations diffuse more slowly than Pb; their compositions
35 784 should reflect conditions of (re)crystallization in all but the smallest grain sizes in the highest
36 785 grade rocks
37 786

[Click here to download Figure Figures.pdf](#)

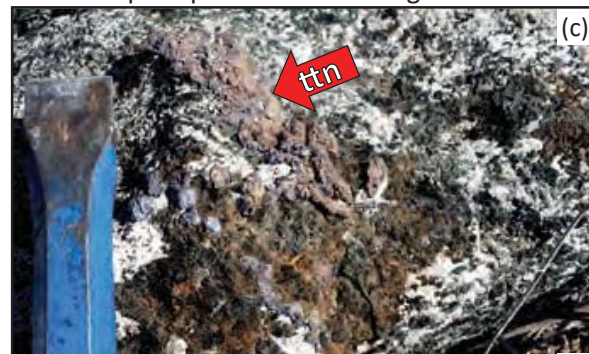
Figures

(b)

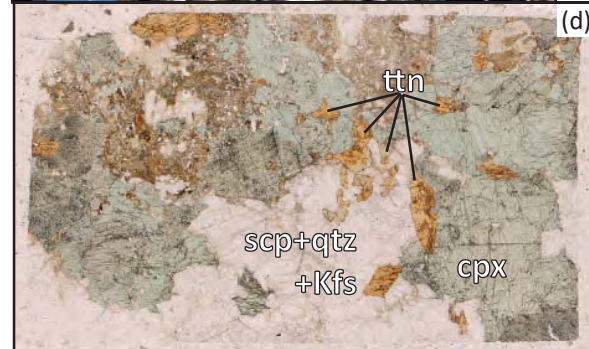
Ptzc =
Proterozoic



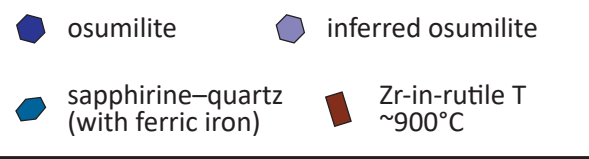
(a)



(c)

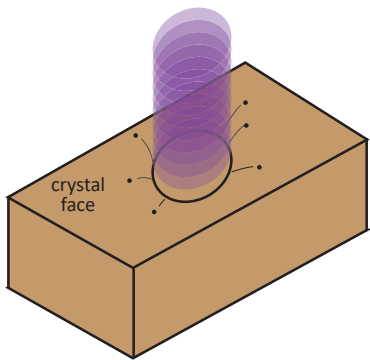


(d)

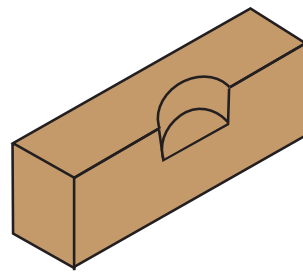
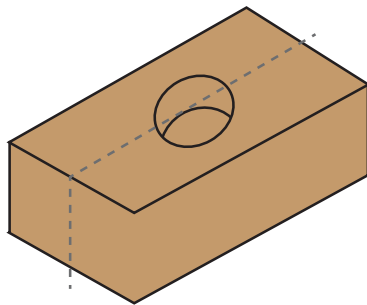


titanite 12D

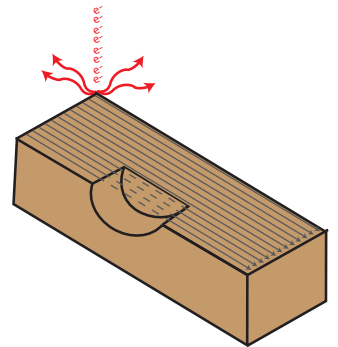
laser-ablation depth profile

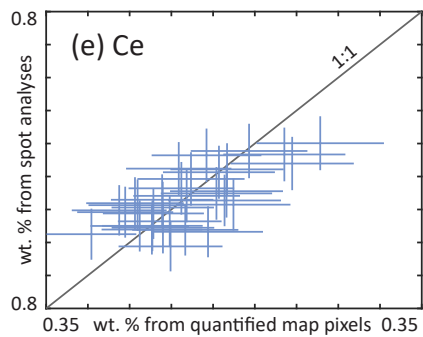
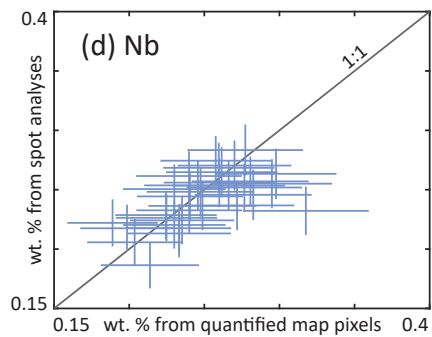
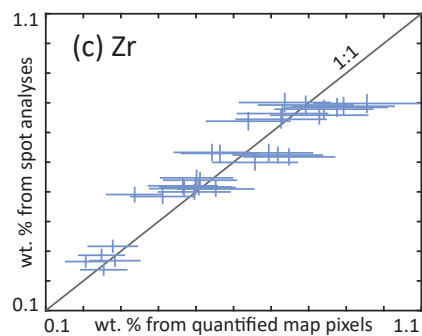
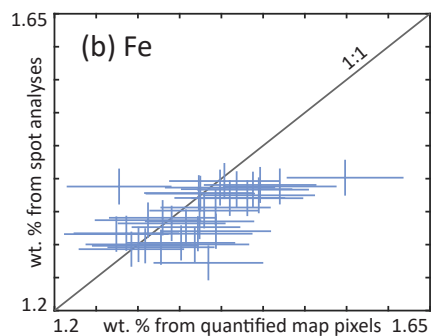
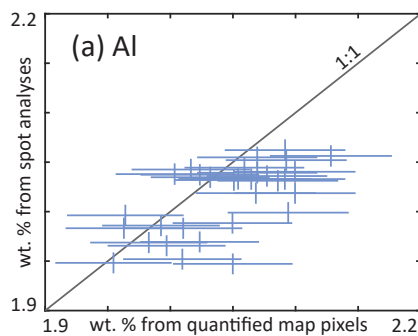


cut perpendicular to grain face

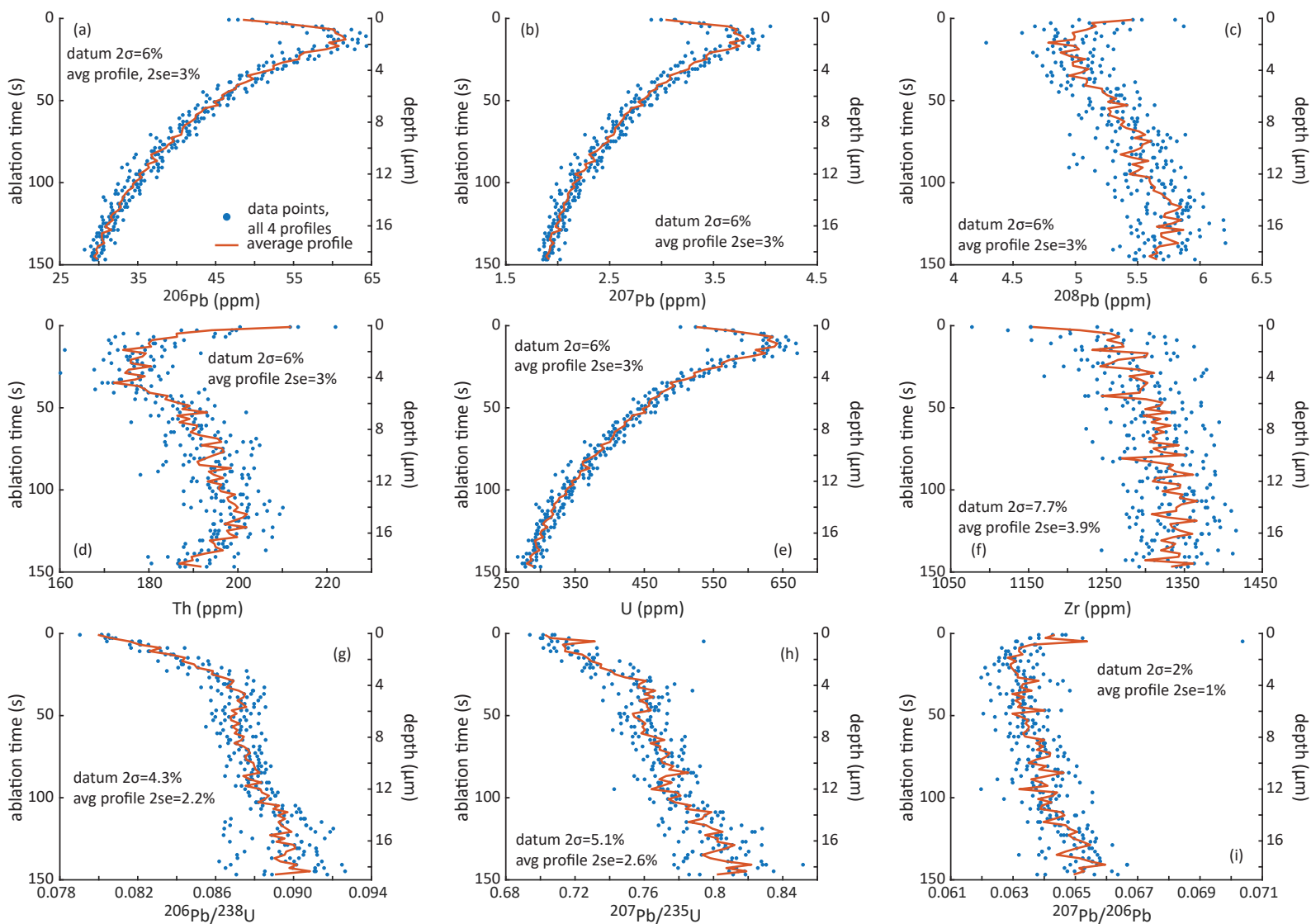


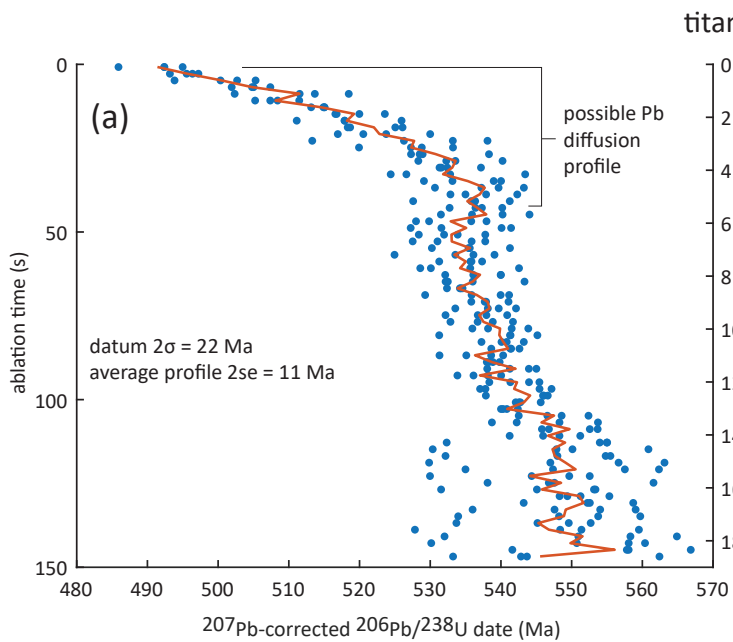
quantitative EPMA map



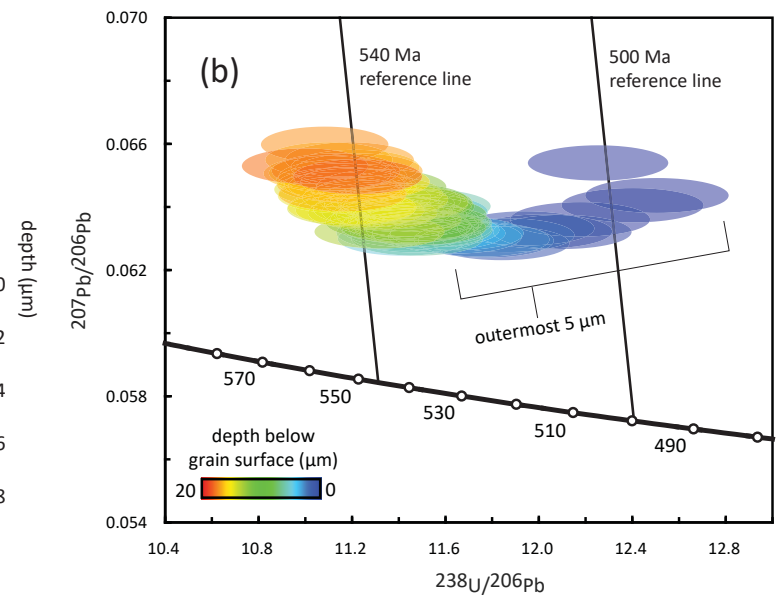


titanite 12D





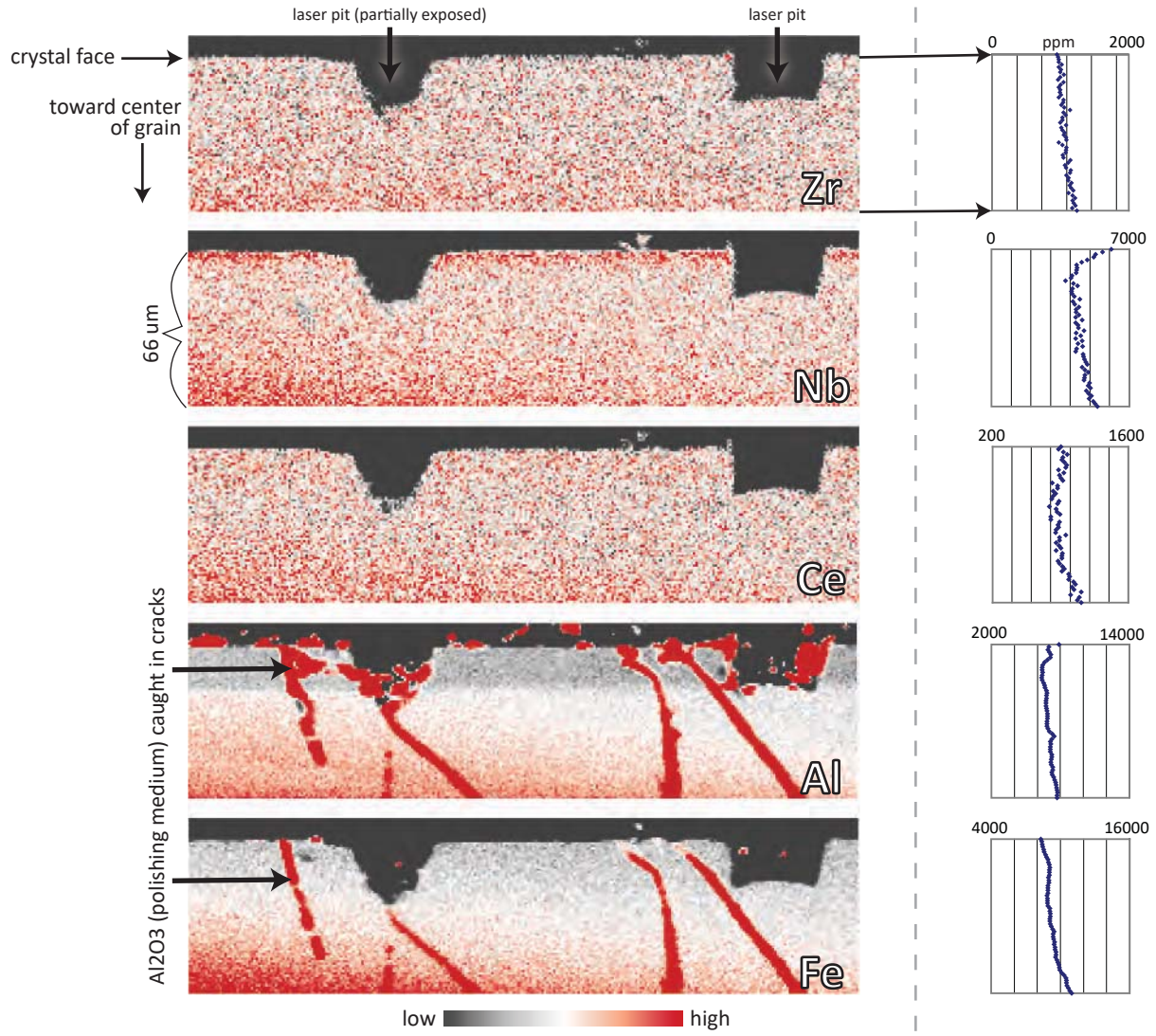
titanite 12D

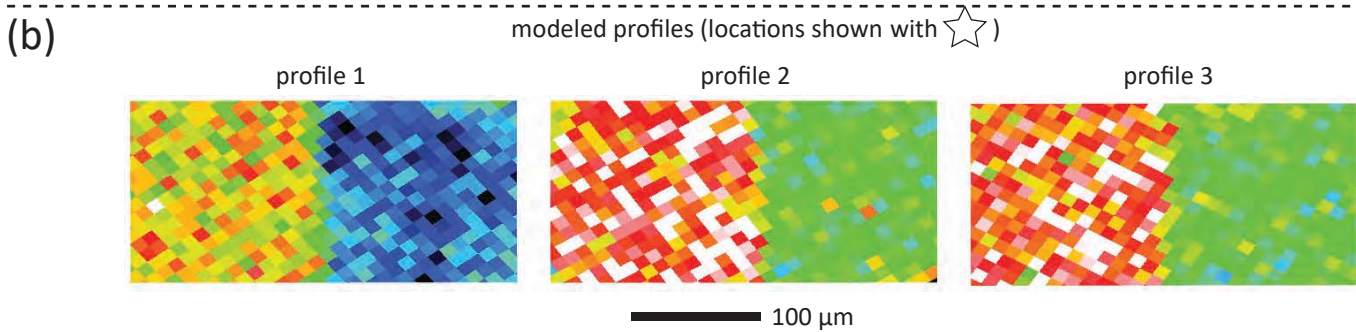
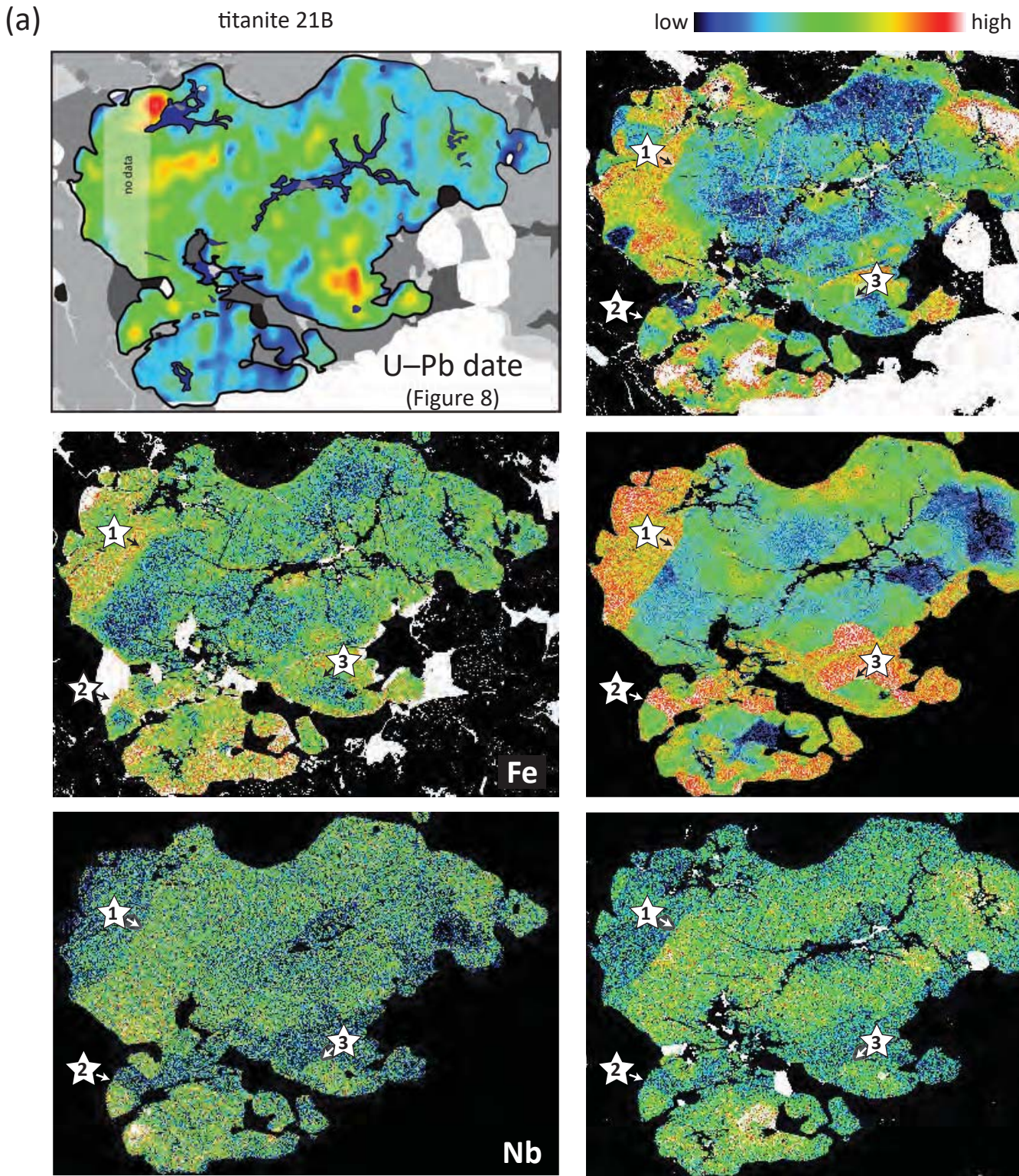


titanite 12D

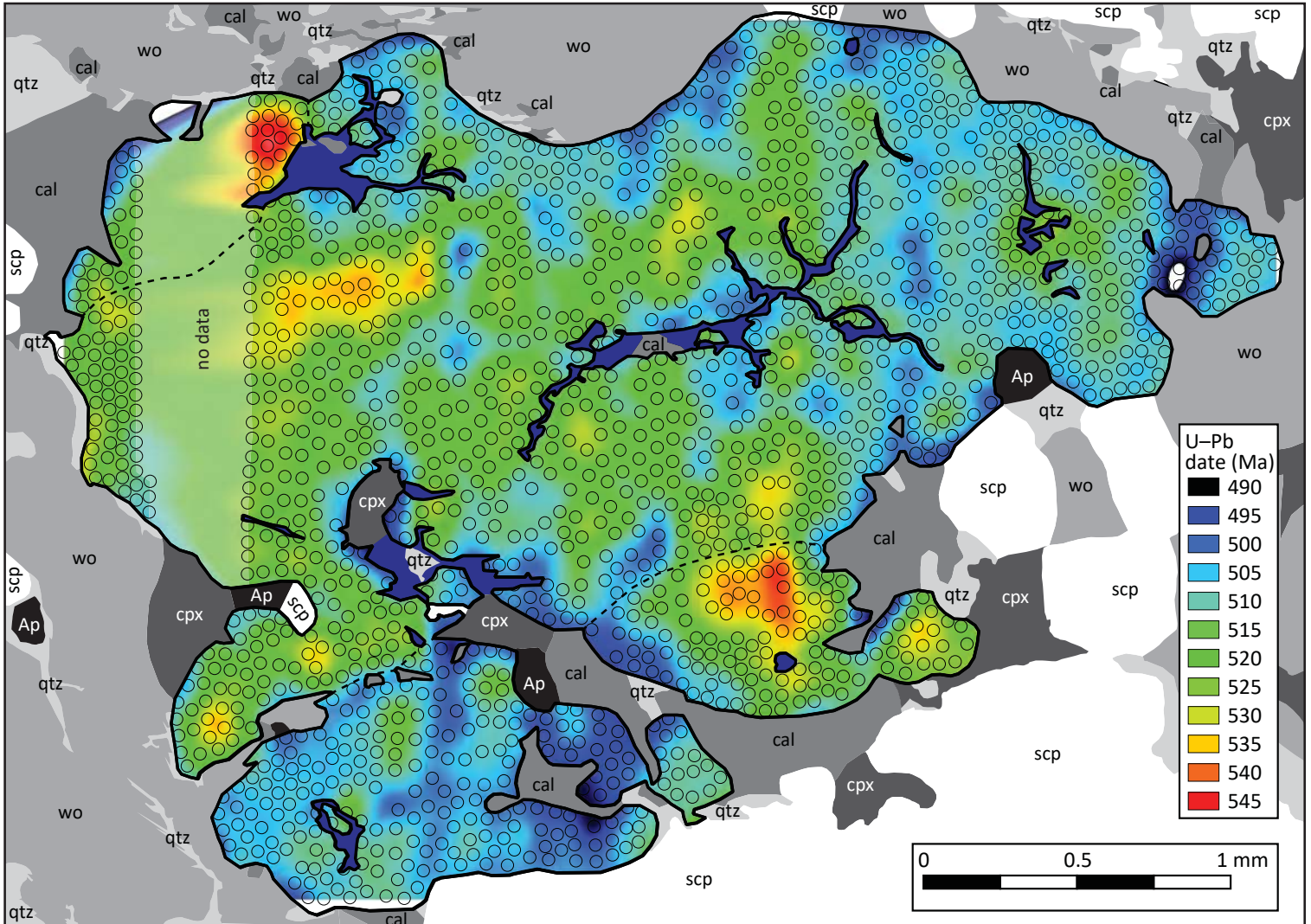
(a)

(b)





titanite 21B



fractures in titanite with abundant inclusions of zircon (high Zr spots in Fig. 7 maps), allanite (high Fe–Al–Ce spots in Fig. 7 maps), and calcite (low Zr–Fe–Al–Ce–Nb in Fig. 7 maps)

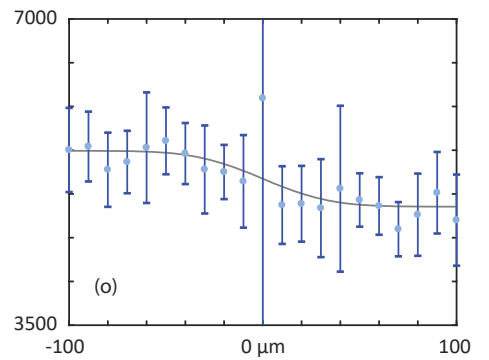
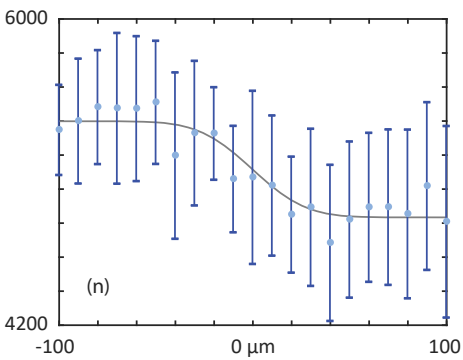
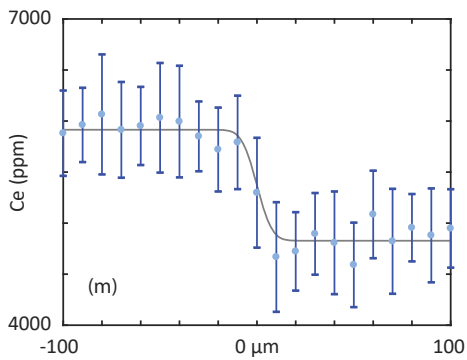
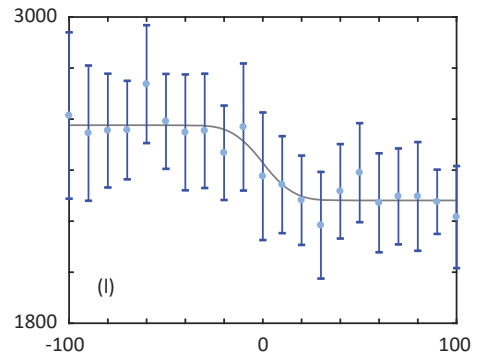
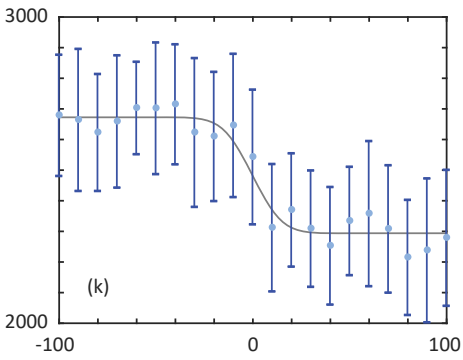
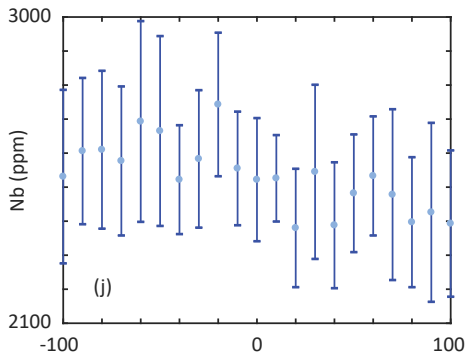
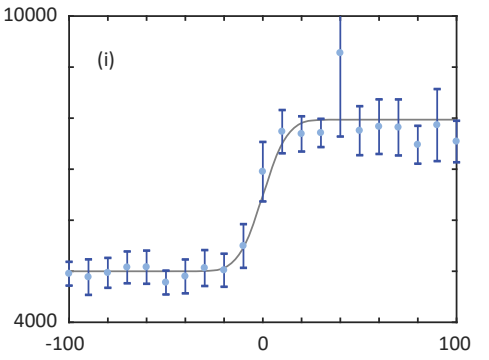
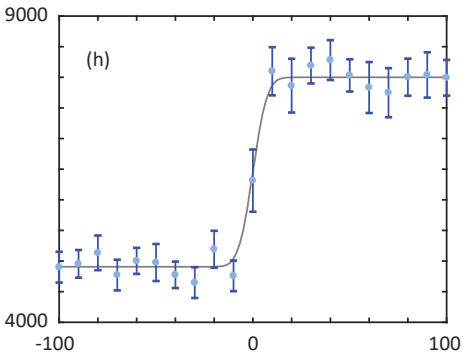
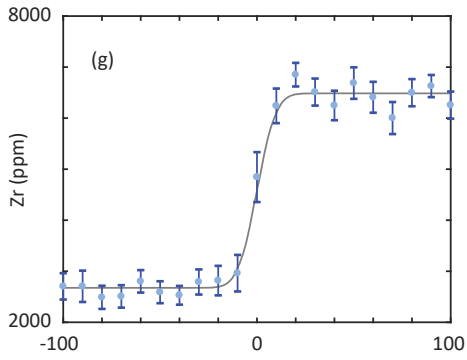
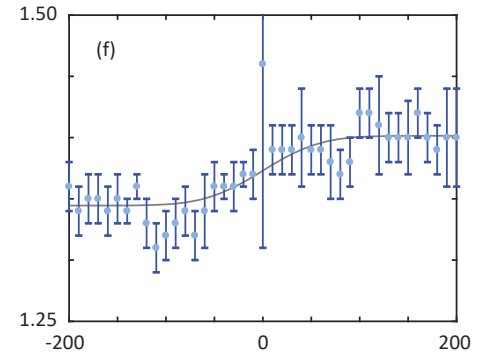
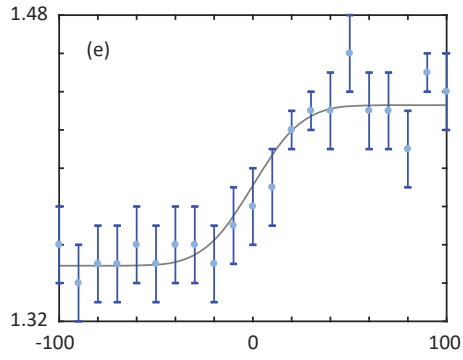
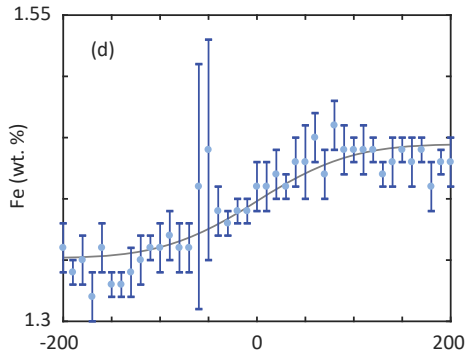
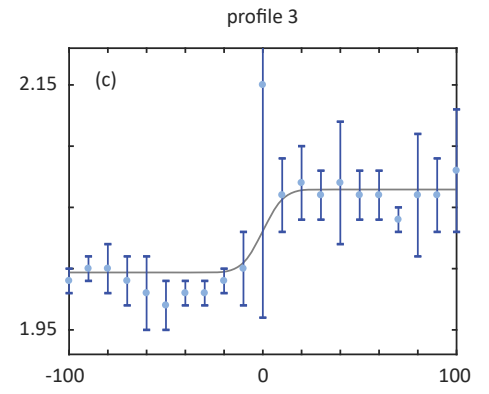
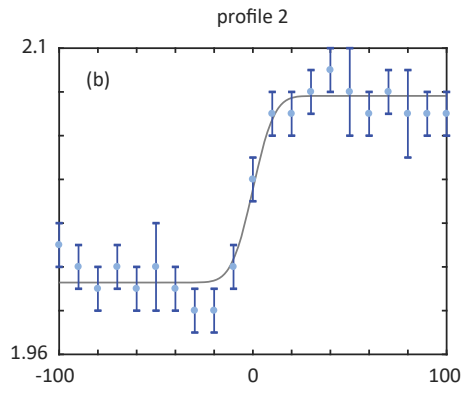
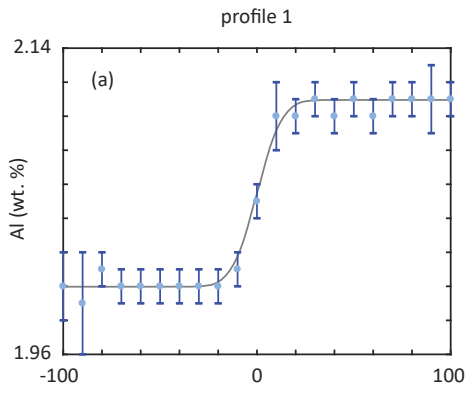


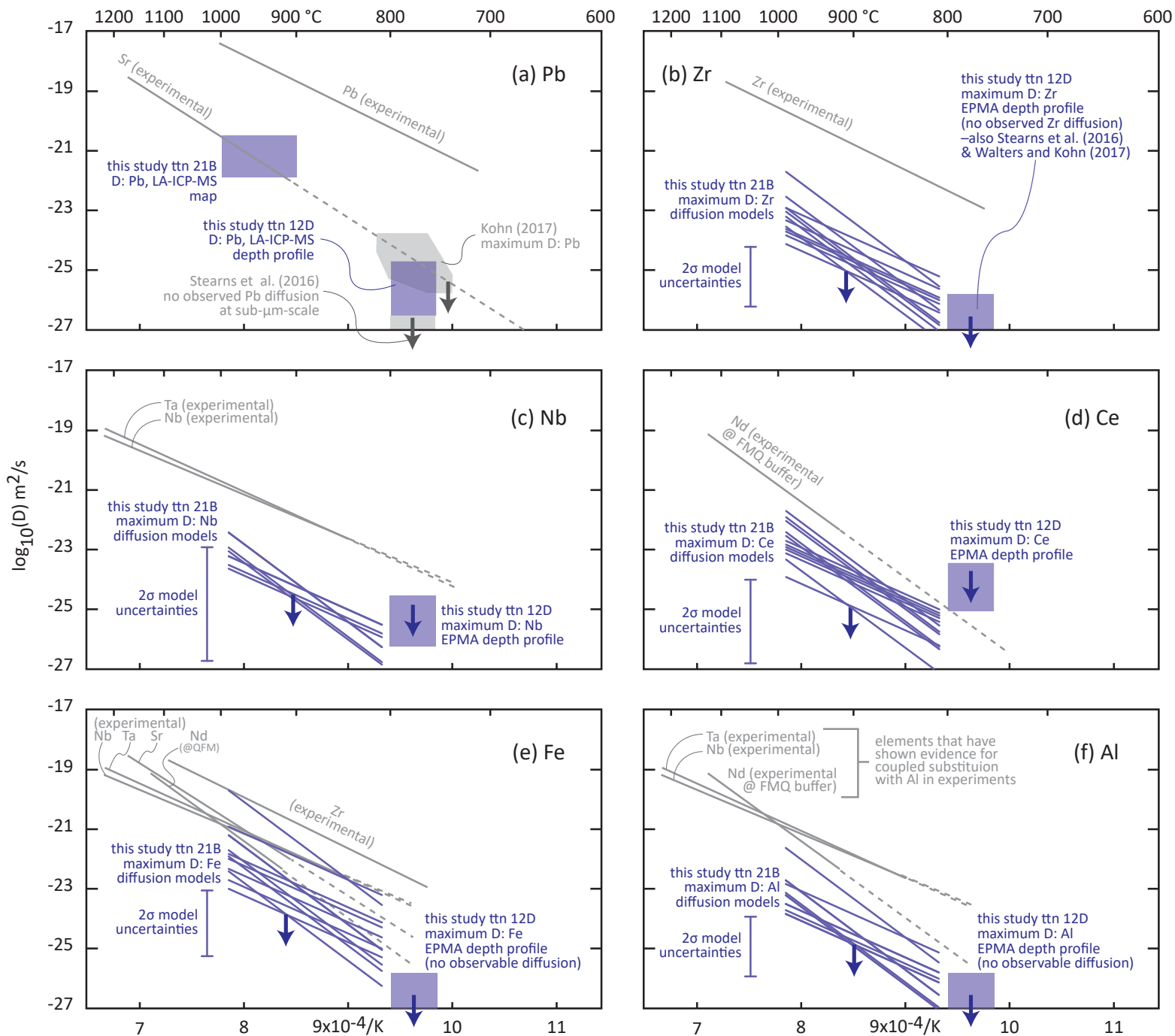
subgrain boundaries (abrupt changes in extinction angle in cross-polarized light)



LA-ICP-MS spot analyses (40 μm diameter)

titanite 21B





	cations									
elemental wt%	Al	2 σ	Si	2 σ	Ca	2 σ	Ti	2 σ	Mn	2 σ
12D	0.71	0.01	14.78	0.23	20.41	0.07	21.54	0.03	0.08	0.01
21B (low Zr)	2.02	0.01	13.35	0.20	20.08	0.07	18.68	0.03	—	—
21B (high Zr)	2.04	0.01	14.82	0.23	20.23	0.07	18.24	0.03	—	—
oxide wt%	Al ₂ O ₃	2 σ	SiO ₂	2 σ	CaO	2 σ	TiO ₂	2 σ	MnO	2 σ
12D	1.35	0.02	31.61	0.48	28.56	0.10	35.94	0.06	0.10	0.01
21B (low Zr)	3.81	0.02	28.56	0.44	28.10	0.10	31.15	0.05	—	—
21B (high Zr)	3.85	0.02	31.71	0.48	28.30	0.10	30.43	0.05	—	—
formula	Al		Si		Ca		Ti		Mn	
12D	0.05		1.02		0.99		0.87		0.00	
21B (low Zr)	0.15		0.95		1.00		0.78		—	
21B (high Zr)	0.15		1.01		0.97		0.73		—	

									anions		
Fe	2σ	Zr	2σ	Nb	2σ	Ce	2σ		O	F	2σ
0.96	0.02	0.13	0.02	0.09	0.02	0.08	0.03		40.54	0.31	0.03
1.34	0.03	0.24	0.02	0.25	0.02	0.59	0.04		38.37	1.61	0.04
1.38	0.03	0.79	0.03	0.21	0.02	0.48	0.04		40.01	1.63	0.04
Fe2O3	2σ	ZrO2	2σ	Nb2O5	2σ	Ce2O3	2σ	total			
1.37	0.03	0.17	0.03	0.13	0.03	0.10	0.04	99.64			
1.91	0.04	0.32	0.03	0.36	0.03	0.69	0.05	96.53			
1.97	0.04	1.06	0.04	0.30	0.03	0.56	0.05	99.83			
Fe		Zr		Nb		Ce			O	F	OH
0.03		0.00		0.00		0.00			4.92	0.03	0.05
0.05		0.01		0.01		0.01			4.80	0.17	0.03
0.05		0.02		0.00		0.01			4.81	0.16	0.03

sample	element	T °C	D $\log_{10} (m^2/s)$	2σ
12D	Pb	750–800	–24.7 to –26.2	—
	Al, Fe, Zr	750–800	≤ -25.8 to –27.4	—
	Nb	750–800	≤ -24.5 to –26.2	—
	Ce	750–800	≤ -23.5 to –25.1	—
21B	Pb	900–1000	–20.5 to –21.9	—
	Al profile 1	900	–24.8	1.0
	Al profile 1	900	–23.9	1.0
	Al profile 2	900	–24.9	1.0
	Al profile 2	900	–24.6	1.0
	Al profile 3	900	–24.9	1.2
	Al profile 3	900	–24.6	1.2
	Fe profile 1	900	–22.9	1.1
	Fe profile 1	900	–22.0	1.1
	Fe profile 2	900	–24.1	1.1
	Fe profile 2	900	–23.8	1.1
	Fe profile 3	900	–23.4	1.1
	Fe profile 3	900	–23.1	1.1
	Zr profile 1	900	–24.9	1.0
	Zr profile 1	900	–24.0	1.0
	Zr profile 2	900	–25.2	1.0
	Zr profile 2	900	–24.8	1.0
	Zr profile 3	900	–24.7	1.1
	Zr profile 3	900	–24.4	1.1
	Nb profile 2	900	–24.7	1.8
	Nb profile 2	900	–24.3	1.8
	Nb profile 3	900	–24.6	1.9
	Nb profile 3	900	–24.3	1.9
	Ce profile 1	900	–25.0	1.4
	Ce profile 1	900	–24.0	1.4
	Ce profile 2	900	–24.1	1.4
Ce profile 2	900	–23.8	1.4	
Ce profile 3	900	–24.2	1.9	
Ce profile 3	900	–23.9	1.9	

starting T used in 21B calculations		21B calculations: $\log_{10} D_0 = m \times E_a + b$			
$^{\circ}\text{C}$	2σ	m	2σ	b	2σ
—	—	—	—	—	—
—	—	—	—	—	—
—	—	—	—	—	—
—	—	—	—	—	—
—	—	—	—	—	—
939	62	0.044	0.003	-24.6	0.4
873	57	0.047	0.003	-24.6	0.4
956	64	0.044	0.003	-24.7	0.3
919	61	0.045	0.003	-24.7	0.4
953	64	0.044	0.003	-24.7	0.7
919	60	0.045	0.003	-24.7	0.7
939	62	0.044	0.003	-22.7	0.5
873	57	0.047	0.003	-22.7	0.5
956	64	0.044	0.003	-23.9	0.5
919	61	0.045	0.003	-23.9	0.5
953	64	0.044	0.003	-23.2	0.6
919	60	0.045	0.003	-23.2	0.6
939	62	0.044	0.003	-24.7	0.3
873	57	0.047	0.003	-24.7	0.3
956	64	0.044	0.003	-25	0.3
919	61	0.045	0.003	-24.9	0.3
953	64	0.044	0.003	-24.5	0.4
919	60	0.045	0.003	-24.5	0.5
956	64	0.044	0.003	-24.5	1.5
919	61	0.045	0.003	-24.4	1.5
953	64	0.044	0.003	-24.4	1.6
919	60	0.045	0.003	-24.4	1.5
939	62	0.044	0.003	-24.8	1.0
873	57	0.047	0.003	-24.7	1.0
956	64	0.044	0.003	-23.9	1.0
919	61	0.045	0.003	-23.9	1.0
953	64	0.044	0.003	-24.0	1.6
919	60	0.045	0.003	-24.0	1.6

difference in D between calculations and experiments	
$\log_{10} (\text{m}^2/\text{s})$	2σ
-4.7 to -6.2	—
-3.7 to -5.3	—
-1.4 to -3.1	—
same as Nd at FMQ	—
-1.9 to -4.4	—
—	—
—	—
—	—
—	—
—	—
—	—
—	—
—	—
—	—
—	—
—	—
-4.2	1.1
-3.3	1.1
-4.5	1.1
-4.1	1.1
-4	1.2
-3.7	1.2
-2.9	1.9
-2.5	1.9
-2.8	2.0
-2.5	2.0
-2.2 (Nd at FMQ)	1.5
same as Nd at FMQ	—
same as Nd at FMQ	—
same as Nd at FMQ	—
same as Nd at FMQ	—
same as Nd at FMQ	—